ANNUAL REPORT

SUBMITTED TO:	National Aeronautics and Space Administration Langley Research Center Hampton, Virginia 23665
INSTITUTION:	Department of Physics and Engineering Studies Hampton Institute Hampton, Virginia 23668
TITLE OF GRANT:	Local Effects of Partly - Cloudy Skies on Solar and Emitted Radiations
GRANT NUMBER:	NAG-1-87
PERIOD COVERED BY THIS REPORT:	August 1, 1980 to July 31, 1981
CO-PRINCIPAL INVESTIGATORS:	D. A. Whitney D. D. Venable
RESEARCH ASSOCIATE:	T. J. Griffin

LOCAL EFFECTS OF PARTLY-CLOUDY SKIES ON SOLAR AND EMITTED RADIATIONS

D. A. Whitney
Department of Physics and
Engineering Studies

ABSTRACT

The first year of the proposed three year research project has now elapsed. Solar radiation measurements are now being made on a routine basis. Global solar, atmospheric emitted, downwelled diffuse solar, and direct solar radiation measurement systems are now fully operational with the first two already in routine continuous operation. Fractional cloud cover measurements can be made from GOES imagery or from ground based whole sky photographs. Normalized global solar irradiance values for partly-cloudy skies have been correlated to fractional cloud cover. Phase I objectives have been attained for global and atmospheric emitted radiation.

TABLE OF CONTENTS

INTRODUCTION

The first year of the proposed three-year research effort has now been completed. The main objective of the initial grant period was to correlate fractional cloud cover with various components of downwelled solar radiation. A measurement program was initiated to provide data for the development and testing of later phases of this project.

There are three essential components to this first phase of the project: (1) solar and atmospheric radiation measurements; (2) fractional cloud cover determinations; and (3) data analysis and correlations. The progress made in each of these components is discussed in detail in the following sections.

I. SOLAR RADIATION MEASUREMENT PROGRAM

The site for solar and atmospheric radiation measurements was established at the Physics Department building, Turner Hall, on the campus of Hampton Institute - latitude 37.02° N, longitude 76.31° W, and elevation 24 meters. The radiation sensors are located at the top of an observation tower (Figures 1 and 2) which was built to obtain an unobstructed field of view for the radiation sensors. A field of view survey from atop the tower, showed that only two obstructions, a radio tower and a smoke stack, have elevations above the horizon greater than five degrees. There are no obstructions higher than ten degrees in elevation. The tower is six meters in height and was constructed with weather-treated lumber for durability. At the top of the tower, one meter above a standing platform, there is a five square meter working surface which provides room for up to six radiometers and an all sky camera assembly. The observation tower was completed February 15, 1981.

Electrical power connections for 110 V ac is scheduled for installation during August 1981. This installation was projected for the spring but has been delayed. Electricity is needed to supply power to operate the solar trackers, radiometer control units, and other support instrumentation. Extension cords are presently being used to provide power. Bendix weather-proof electrical connectors and individually shielded signal cables were installed leading from the sensors to the recording system in the solar measurement laboratory located on the third floor of Turner Hall. Preliminary instrumentation checkouts were conducted during December 1980 and January 1981. The available instrumentation, data handling procedure, data storage and quality control are discussed in the sections below.

A. Instrumentation

The instrumentation chosen for this project will provide accurate ground based measurements of solar and atmospheric radiation. Instrumentation to obtain atmospheric turbidity and precipitable water is also available. Table I lists the available instrumentation as well as the measurement wavelength ranges. Table II shows our measurement capability and sampling information

1. The Eppley Precision Spectral Pyranometer (PSP)

There are two Eppley PSP s available to obtain measurements of global solar and diffuse solar irradiance in the wavelength range of 0.285μm to 2.8μm. The Eppley PSP is a durable instrument with an accuracy of $\pm$ 2% for solar zenith angles ranging from 0 to 70 degrees, and temperatures ranging from -20°C to 40°C. It has a time constant of one second. This instrument is widely used in DOE (Ryzner) and NWS (Baker) solar measurement networks. The maintenance schedule for the Eppley PSP includes daily cleaning of the glass dome, checking for levelness, and periodic changing of the desicant. The Eppley PSP can be seen in Figure 1 at the far left of the platform.

Global solar radiation is the combination of downward direct and diffuse solar radiation as received on a horizontal surface within a solid angle of 2 π steradians. Global measurements have been made on a continuous basis since February 17, 1981. Several minor interruptions in continuous measurement have been caused by electrical power failures, system calibrations, and routine maintenance.

Diffuse solar radiation measurements are performed with the Eppley PSP shaded from the direct solar beam by using a shadow band, or by using an occulting disk mounted on a solar tracker. The occulting disk tracker instrument requires a special support unit to allow the tracker

to rotate the disk 360° around the PSP without obstruction during each twenty-four hour period. This assembly is shown in Figure 2 and is located at the northeast corner of the platform. The occulting disk instrument is used at this station to measure diffuse radiation because it eliminates the uncertainty involved in applying shadow band corrections which are only valid for "average cloudy conditions" (Drummond, Eppley).

The occulting disk-solar tracker assembly was installed in June. Diffuse radiation measurements have been made on a part-time basis to properly align the solar tracker system. Tracking from sunrise to sunset requires exact alignment in the north-south direction, as well as the exact declination and latitude settings. Continuous operation is expected to begin in August 1981 when electrical power is permanently available at the measurement platform in weatherproof outlets.

2. The Eppley Precision Infrared Radiometer (PIR)

The Eppley PIR is used to obtain measurements of downward atmospheric or longwave radiation in the wavelength range of 4.0μm to 50μm. To protect the sensor, the instrument uses a silicon hemisphere which is uniformly transparent over the region of 1μm to 40μm. An interference filter, with a transmittance cut off between 3 microns and 4 microns is vacuum deposited on the inner surface of the silicon hemisphere. The sensor incorporates a battery operated temperature compensation circuit to compensate for radiation lost due to sensor temperature. It has an accuracy of $\pm$ 7% for all solar zenith angles and a working temperature range of -20°C to 40°C. In Figure 1, the PIR is the second instrument from the left.

Atmospheric infrared radiation measurements have been made on a continuous basis since March 18, 1981. The regular maintenance schedule includes daily cleaning of the hemisphere and checking of the level. Monthly checks

of battery output and desicant are also performed. A few power failures, a battery failure, and scheduled calibrations have interrupted continuous measurement.

3. The Eppley Normal Incidence Pyrheliometer (NIP)

The Eppley NIP is used to measure direct solar radiation in the wavelength range 0.285μm to 4.5μm. The instrument is designed so that only direct radiation from the sun and some circumsolar radiation is permitted to fall on the receiver. The circumsolar radiation results from the fact that the field of view of the instrument is 5.7 degrees while the sun subtends an angle of only 0.5 degees. The instrument has an accuracy of ± 1% from $-20^{\circ}C$ to $40^{\circ}C$. Spectral components of direct solar radiation can be measured using a filter wheel mounted on the front of the instrument. The NIP is shown in Figure 1 at the far right.

Measurements of direct radiation have been made periodically since May. Continuous measurements will begin in August when the permanent ac power is installed. Regular maintenance includes daily declination alignment and lens cleaning.

4. The Eppley Hickey-Frieden Absolute Cavity Pyrheliometer

An Eppley H-F pyrheliometer has been obtained for sensor calibrations and future experimental work. It incorporates a self-calibrating sensor and control unit. The sensor is the same type as that employed in the solar constant monitor on the NIMBUS-7 satellite. The instrument measures direct solar radiation in the wavelength range of less than 0.2μm to greater than 50μm. It has a 8.5 degree field of view and a time constant of 1 second. This instrument is the same as that used by Eppley Laboratory to calibrate the NIP's. The instrument will not be used on a continuous basis, but will be periodically used for calibration of

other sensors.

5. The Volz Sunphotometer

The Volz Sunphotometer is used to measure turbidity at 500 nm, aerosol extinction coefficients at 390 nm and 875 nm, and for precipitable water. Direct solar radiation is measured using a silicon photocell and narrow band transmission filters centered at 380, 500, 875 and 945 nm. Measurements are made at approximately one hour intervals throughout the day. Before May 1, 1981 data were obtained only for completely clear sky conditions. After that date observations during cloudy conditions were included if there existed no obstruction between the sun and the observer.

6. All Sky Camera System

A Ricoh XR-2, 35 mm SLR camera with an Aetna fisheye adaptor lens is used to take ground based photographs of cloud cover. A red filter and polarizer are used to reduce glare and to increase the contrast between clear sky and cloud cover while a small occulting ball is used to shade the lens from the direct sun. Black and white photographs are scheduled hourly during the measurement period for suitable cloud conditions. Selected photographs are enlarged and analyzed by hand for fractional cloud cover.

B. Meteorological Data

Standard hourly meteorological observations taken at Langley Air Force Base (LAFB) are picked up on a monthly basis from the Third Weather Squadron. These data include information about cloud height, cloud type, and fractional cloud cover and are transferred from the LAFB hard copy onto magnetic tape in proper format for analysis of cloud type frequency, fractional cloud cover frequency, and other related cloud parameters. Visual observations were made at Hampton Institute to accompany the photographs.

C. The Data Acquisition System

The data acquisition system employed to monitor the radiation sensors is shown in Figure 3. It consists of an integrator-printer-recorder system for each of the four measurements; i.e., global, diffuse, direct, and infrared radiations.

Each individual data acquisition system consists of an Eppley integrator matched to the radiometer, a Digitec Printer with built-in timer, and a linear strip chart recorder channel. Each integrator is connected to a radiometer by shielded twisted pair cable and continuously monitors the sensor's output voltage. It converts this voltage into energy received and then displays the integrated energy total on a LED panel. At the same time, the integrator generates an output voltage proportional to the sensor voltage. The linear strip chart recorders are used as a back-up system to supply data when the integrator-printer system malfunctions and as a continuous record of the various solar energy components and atmospheric radiation.

Once an hour the Digitec printers send a signal to the integrators which respond to this signal and transfer the data displayed on the the LED panel back to the printer to be printed on paper tape. At midnight (EST) each day, the integrators reset the LED displays to zero and the printers reset the clocks to zero.

D. Calibrations

Original calibrations of the Eppley PSP's is performed prior to delivery by the Eppley Laboratory using a standard Angstrom pyrheliometer reference. Comparison of our two instruments was made in May when the second PSP arrived from Eppley. Results of this test showed that the daily total irradiance recorded by the two instruments agreed within 1.6% of each other - a variance which is within the instrumental accuracy. Suggested calibration

time is one year for the PSP's. Calibration of our first instrument will be taken care of in October, 1981.

Calibration of the Eppley NIP was performed by the Eppley Laboratory prior to shipment. Once continuous measurements begin, in-house calibration will be performed using the H-F Absolute Cavity Pyrheliometer as the standard instrument. Calibration is scheduled on a six month basis.

Calibration of the Eppley PIR and the Volz Sunphotometer must be made by the manufacturers. Present plans are to return these instruments for calibration at the end of 1981 since each would have been in operation for one year at that time.

The recorder systems are calibrated every two months. The procedure involves using a stable millivolt source to supply a known voltage to each integrator. The integrator count rate and recorder output voltage are compared to specifications. If necessary, resistors inside the integrators are adjusted to meet the specifications set by the Eppley Laboratory.

E. Data Handling and Quality Control

A data storage procedure for the radiation data has been devised to efficiently handle the data and ensure quality control. Printed data from the integrators are scanned on a daily basis for missing or problem data and incorrect timing caused by power failures and other electrical malfunctions. Missing data are supplemented by the strip chart record when available. The data storage scheme in Phase I of the project does not call for automation. This will be a major objective of the second phase. The data storage process was established to be consistant with the data automation scheme that will be implemented in the next phase.

Currently all radiometric data from integrators are printed on paper tape each hour of the day. On a weekly basis, these data are manually

entered into a Tektronix 4051 microcomputer and stored on that computer's internal tape unit. The raw data files include integrated radiometric readouts and the corresponding times. A computer file is generated for each day and for each instrument. The 4051 tapes serve as a temporary storage medium for these data. For permanent storage the taped information is transferred via computer hookup from the 4051 to the PDP 11/34 minicomputer where data are stored on 1600 bpi magnetic tape. All preliminary processing is done on the Tektronix 4051. Data analysis routines are done on the PDP 11/34 system.

Meteorological data are stored directly on the PDP 11/34 magnetic tape system, and these data files contain hourly weather observations for a twenty-four hour period. All application programs utilizing these data are operated on the PDP 11/34.

II. FRACTIONAL CLOUD COVER DETERMINATION

The largest single effect of a cloud upon the solar radiation received at the ground is caused by partial occlusion of the direct beam by an opaque cloud. The cloud's type, density, thickness, height and reflectivity also affect the energy received at the ground. Cloud cover composed of cumuliform clouds was selected for this study because of the nearly opaque optical properties, low cloud altitude, distinct boundaries, and frequency of occurence. Cloud cover measurements were usually not made when cirrus, cirrostratus, or semi-transparent altocumulus clouds were present. With this in mind, the term "cloud cover" will be used to mean opaque cloud cover as opposed to total sky cover.

Fractional cloud cover can be defined for a local area by the ratio of cloudy area to total area, or by cloudy solid angle to total solid angle. The area ratio should be valid for large ground areas or for time averaged

small areas as the clouds move around. Solid angle weighting could be useful for small area and short time period measurement comparisons; but is not compatible with satellite viewpoints unless cloud altitude is readily found. For these reasons all fractional cloud cover measurements are based upon the definition that fractional cloud cover equals the ratio of the area obscured by clouds to the total area.

There are three different sources of fractional cloud cover values: (1) satellite data, (2) ground based photography, and (3) trained observers.

A. Satellite Derived Cloud Cover

Satellite data can be used to determine fractional cloud cover by either of two main methods. The raw brightness data from each channel of each sensor can be manipulated, interpreted, and compared to the corresponding data for clear and totally cloudy conditions. The other method involves the analysis of satellite imagery such as photoprints. Photoprints are generated from the raw data and are readily available in either positive or negative forms for visible and infrared data. The latter approach was chosen for the initial grant period since photos are easier to interpret and work with.

1. Data Selection

Several sources of satellite imagery were investigated. These included GOES, Landsat, TIROS-N, and NIMBUS. Imagery provided by GOES East was selected subject to the requirements of (1) frequency (half-hourly prints are available whereas Landsat makes only one pass every 18 days), (2) full cloudiness range, and (3) convenience (our local geography is easily distinguishable in the visible photos). GOES East-sector DA-1, visible channel, 10"x10" matte finish photoprints are ordered from the National Climatic Center, Satellite Data Services Division in Washington,

D.C., as needed to supplement and/or compare to our ground based fractional cloud cover measurements.

2. Photoprint Grid Design

The GOES East geosynchronous satellite is located 1^{o} east and 37^{o} south of our measurement site at a height of 3.6×10^{7} meters. This view of the local area causes a difference between the north-south and east-west distance scales on the photo. A simple trigonometric calculation predicts that the local zenith direction is 42.5^{o} from the local GOES satellite viewing direction. This introduces a scale factor difference of 1.36; i.e., the north-south scale factor divided by the east-west scale factor equals $1/\cos 42.5^{o}$. The local horizon is circular in shape as viewed from the ground but is elliptical as viewed from the satellite. The circular delineator and square grids reported in this project's semiannual report (February 1981) were modified to account for this anisotropy.

Careful measurements of distance between local landmarks on the satellite photos were made with a scale that was graduated with 0.1 mm divisions using a 10 X jewelers loope. For the 10"x10" photoprints a scale of 29.5 $\pm$ .3 km/cm along the north-south direction, and a scale of 21.8 $\pm$ .2 km/cm along the east-west direction were obtained (47.5 $\pm$ .5 miles/cm and 35.0 $\pm$ .4 miles/cm, respectively). Using this information an ellipse corresponding to a 120 km radius horizon circle can be drawn by computer on the photoprint or on a clear plastic overlay. This horizon ellipse is then sectioned into grids for analysis with the size of each grid determined by the analysis method. For visual cloud estimation within each grid, a rectangular grid corresponding to a 24x24 km (15x15 mile) square on the ground is used. Use of the densitometer requires a square grid which represents a 32x24 km (20x15 mile) rectangular space on the ground. The circular densitometer

head then corresponds to a 32x24 km ellipse at the ground. Both grids are modifications of the grid reported in the semiannual report. An additional improvement in grid design is the location of the central grid over the measurement site. The central grid and its nearest neighbors correspond more closely to the normal field of view at the ground. A single grid is large enough to include both the primary measurement site at Hampton Institute and the supplementary visual cloud observation site at Langley Air Force Base. The relative positions of these sites with respect to the analysis grid is shown in Figure 4 with an "X" for the Hampton Institute site and a dot "." for the Langley Air Force Weather Office site.

3. Densitometer Analysis

Positive black and white photoprints were chosen because of the ease of discrimination between cloud, land, and sea. Use of the positive prints required the reflection mode of measurement instead of the transmission mode. The 4.0 mm diameter ninety degree reflection head of the Photodyne Model 99XL Densitometer/Reflectometer was held by hand and guided by the 4.3 mm x 4.3 mm square grids within the horizon ellipse. Reflection readings were taken and recorded for each grid on both a partly-cloudy photoprint and on a completely clear sky photoprint with similar ground albedo. The difference between the totals of these readings for partly-cloudy and completely clear prints was compared to the expected difference between completely cloudy and completely clear totals. Thus fractional cloud cover (f) was defined by the linear interpolation between clear and completely cloudy totals; that is,

$$f = \frac{\text{partly cloudy total-clear total}}{\text{completely cloudy total-clear total}}$$

This procedure was found to have several drawbacks which can be categorized as instrumental, photographic, or methodological. The maximum difference between clear and cloudy reflection readings for an individual grid was found to be less than 0.32 with an uncertainty of about 0.02 relative units. Matte finish photos provided more sensitivity than glossy finish prints. The actual measurement area is 1.5 mm in diameter while the sensor head is 4.0 mm in diameter. This size difference allows some additional uncertainty in individual measurements due to positioning within the grid and questions regarding representativeness of the sampled area. Thus, instrumental uncertainties can easily contribute about ten percent of the cloudy versus clear difference. Experimental technique minimizes most of the uncertainties due to head orientation (the maximum reading is assumed to occur for normal incidence) and positioning (the square grids are only a line width larger than the reflectometer head).

Several of the problems that arise from the satellite photo are caused by geographic locator dot placement and sensor resolution. Geographic locater dots are meant to locate state boundaries and major lakes or waterways. These normally white dots are black when placed over a bright cloud field. These dots are not uniform in size from photo to photo and are often placed as far as 80 km (fifty miles) from their intended positions. These position changes affect the location and number of dots within the grids and thus the reflection readings of clear versus cloudy skies. The location of the dots can also affect the location of the central grid relative to the measurement site if only the dots are used for positioning. The graininess of the photo is also related to sensor size and movement. In addition, satellite sensor resolution is about 1 km, which means that small clouds separated by large distances, and small holes in clouds, are sometimes undetected or misrepresented.

The angular dependence of ground and cloud albedo is the primary source of uncertainty inherent in the procedure. A clear day, several days away from the selected partly cloudy photoprint, can produce several degrees in zenith and azimuth difference in the sun's angular position. The effect on overall brightness is evident if two photos one hour apart are compared. The effect of different solar orientations introduces considerable uncertainty in the fractional cloud cover calculation. The completely cloudy totals are also subject to solar orientation dependence as well as individual cloud reflectivity. The brightness of a cloud as viewed from the satellite depends upon such factors as cloud type, density, shape, size, and height above the ground. A considerable range in reflection readings can be obtained for completely cloudy grids.

4. Visual Grid Analysis

The visual grid analysis method is simple, quick, and at least as accurate as the densitometric method. The visible fraction of each grid that is covered by clouds is estimated, then these fractions are averaged. This method is advantageous because only the partly-cloudy photo has to be analyzed. An overlay grid can be centered over the measurement site independent of the locator dots when local geographic features are visible. In addition, the angular dependence of sunlight reflected by the clouds is less important. Fractional cloud cover within each grid can be estimated to the nearest one-tenth, or better, which is more accurate than the densitometric method. The grids can be made rectangular to reduce the north-south bias of the square grids. The cloud cover fraction is estimated over the full grid area instead of a small circle within the grid and is thus more representative of the actual cloud fraction. The visual estimate method has one main source of uncertainty: observer bias, in addition to those

inherent to low cloud and small cloud identification.

5. Results and Conclusions for Satellite Photoprint Analysis

Figure 5 compares visual and densitometric results for an August 25, 1980-1201 EST photoprint and for a March 3, 1981-0901EST photoprint. As the number of grids is increased, both methods show the same behavior. For the August photo, the two methods give the same fractional cloud cover at 36 grids (a 6x6 grid square representing 192 km N-S by 144 km E-W centered over the primary measurement site). Both methods agree within estimated experimental error for the full 68 grid analysis circle. The March photo shows an initial increase from clear to cloudy and a general increase as more and more grids are included for both methods. The difference in magnitude can be assigned to the uncertainty in the clear sky values since several clear reference grids had higher reflection readings than the corresponding partly cloudy grids. Using the average difference over these clear grids as a correction for every grid yields a 5 percent cloud fraction for the 51 grid ellipse. This agrees very well with the 7 percent cloud fraction obtained visually; however, this adjustment would produce a negative fraction for the central grid alone.

The difficulties in obtaining reliable fractional cloud cover from the reflection readings led to the conclusion that the visual estimate method was the preferred analysis method. Subsequent satellite photos have all been analyzed by the visual estimation method using the rectangular grids centered over the primary measurement site. Comparisons of satellite derived fractional cloud cover to ground based values will be made below.

B. Ground Based Fractional Cloud Cover

Fractional cloud cover can be obtained from the ground by visual estimation from trained observers or from whole sky photographs. Visual esti-

mates are available from trained observers at the Weather Office of the Langley Air Force Base, Third Weather Squadron. These estimates are made hourly and a copy of these observations is obtained on a monthly basis to supplement the photographs made at the primary measurement site. Only cloud fractions estimated for cumuliform cloud cover is used in the data analysis. Whole sky photographs are taken at the primary measurement site as discussed in the semiannual status report (February 1981). A Ricoh XR-2, 35mm SLR camera with an Aetna fish-eye adaptor lens photographs all the visible sky within an effective angle of 85° from the zenith. Visual cloud estimates at Hampton Institute were made to accompany many of the photographs.

1. Calibration of the Fish-Eye Lens

The relationship between image location on the film and the object's original position or direction had to be ascertained before an analysis grid could be designed. A direct relationship was expected (Lund and Shanklin, 1972) between an object's angular position and the distance from the corresponding image to the center of the photograph. Preliminary testing of the camera and fish-eye lens combination indicated that the maximum practical angular view was about 85° from the principal axis of the lens system. A calibration experiment was conducted to test this range and to test the linearity of the image position versus the object direction. A classroom wall was selected as the object since a flat surface of considerable size was required. The width of the wall was 6.1 m (20 feet) and the height was 2.4 m (8 feet). The camera to wall distance was set at 26.7 cm (10.50 inches) so that the intersection of the walls would be 85.0° in the horizontal direction. Using this set distance, positions were calculated for twenty angles. For every five degrees below 40°, circles were drawn on a 10"x15" sheet of paper by computer. For angles greater than 40°, positions were marked on the wall by hand for every 45° in azimuth. Figure 6 is a copy

of one of the calibration photos. The bright spots along the 0^{o} and 180^{o} directions are the 85^{o} positions illuminated. Additional points for the calibration were obtained by using the very regular spacing of the building blocks. Measurement of all these positions on the two calibration photos provided 39 data points with experimental uncertainties determined by comparing the two photos and the different directions for the same orientation angles. The uncertainties were used in the statistical weighting for the linear least-squares fit to the data. A slight discrepancy was observed for points above the camera versus points below the camera. This was attributed to a slight vertical misalignment of the camera system which was leveled by the use of a small bubble level.

Figure 7 shows the distance of the image from the center of the photo versus the angular orientation of the object for the calibration of the whole sky camera system. The position of an image is a linear function of the object's angular position as seen in this figure. The scale factor is a function of the size of the enlarged photograph and is not particularly significant. The important thing is that the edge of the circular photo is 85.0^{o}, the center is 0^{o}, and any position between the center and the outside edge is linearly related to the angular position of the object.

2. Analysis Grid Design

The symmetry of the photographs and the object angle-image position dependence suggest that a series of concentric rings divided into equal segments be used instead of a rectangular grid pattern. A similar grid was developed by Lund and Shanklin (1980). The practical limit of 85^{o} from zenith means that only clouds nearby the primary measurement site can be photographed. This range is only a few kilometers for very low cumulus clouds and about 50 km for altocumulus and other middle level clouds. In

relation to the satellite photo, only clouds within the central grid are visible in the ground-based photo for low clouds, and one or two grids from the center for higher clouds. This small region near the earth's surface can be treated as being flat as long as the clouds all have the same base altitude. The distance R from the zenith direction and the cloud height h are related by $R = h \tan \theta$, where theta can be determined from the photograph. The area of a ring segment is a fraction of the total ring area $\pi(r_2^2 - r_1^2) = \pi h^2 (\tan^2\theta_2 - \tan^2\theta_1)$ and the total area represented in the photo is $\pi h^2 \tan^2 85^\circ$. Fractional cloud cover f for a ring can be taken as the average fractional cloud cover for that ring. Thus $f = \frac{1}{n}\sum_{j=1}^{n}(f_j)$ where n is the number of equal segments and f_j is the fractional cloud cover for the j-th segment. The fractional cloud cover F for the entire circular field of view is equal to the total cloudy area divided by the total area. This definition becomes

$$F = \frac{\sum_{i=1}^{N} \pi h^2 f_i (\tan^2\theta_i - \tan^2\theta_{i-1})}{\pi h^2 \tan^2\theta_N}$$

The total area only depends upon the angle θ_N of the last ring used and the cloud height. This last ring represents 85° if the full sky photo is used. Thus the final fractional cloud cover for N rings is equal to a weighted sum of individual ring cloud fractions; that is,

$$F = \sum_{i=1}^{N} (f_i w_i) \text{ with } w_i = \frac{(\tan^2\theta_i - \tan^2\theta_{i-1}}{\tan^2\theta_N}$$

For $i = 1$, set $\theta_{i-1} = \theta_0 = 0$ since the first "ring" is a circle of radius h x $\tan \theta_1$. Note that w_i does not depend on cloud height as long as the height for all clouds is the same throughout the view of the camera.

Angular positions for equally weighted rings were calculated and found to be impractical since these areas all fall near the outside edge of the photo. Practical estimation of cloud cover over a section of a circle or ring requires that the areas be relatively small. The final analysis grid is shown in Figure 6 (page 33). Seven rings, chosen for convenient ring size and angles, were segmented radially into eight equal segments. The angles and corresponding weighting factors are listed in Table III using all seven rings for the weight factor calculation. The dotted circles divide the first six rings into half areas. The lighter sector lines divide each segment in half. The half area lines are used to reduce the uncertainty in estimating cloud cover over each section to about five percent. The outermost ring is not divided in half by a dotted line because the half area line nearly overlaps the outer ring. The weight factor for the outside ring is very large, thus the outside ring (and any errors in its evaluation) strongly influences the final fractional cloud cover. This outer region of the photo is also where the sides of clouds are most noticeable. Most cloud fractions reported here are calculated using only the first five rings and the appropriately modified weighting factors. The outer two rings are only used for very small fractional cloud cover when the clouds are usually near the horizon and sparsely distributed in space.

As a preliminary test of the photographic analysis technique, two photos of a rapidly changing cloud pattern were taken at slightly different times. Figures 9 and 10 are copies of photographs taken at 1350 and 1355 EST on February 25, 1981. The movement of the clouds is evident as shown by the relative size and location of the clear sky regions. Analysis of the two photos produced cloud fractions of 59% for the 1350 EST photo and 57% for the 1355 EST photo. An independent analysis of the 1355 EST photo by a student assistant produced a value of 55%. A similar analysis of two

photos taken April 6, 1981 at 1400 and 1406 EST produced 80 and 82%, respectively. It was concluded that the analysis technique was correct.

The primary drawbacks for the method are related to the correct identification of cloud edges, sides and bottoms in the black and white photographs. A dark cloud bottom is not readily distinguishable from a clear area when it is at an angular position greater than about 60°. Cloud sides can also appear to be as large as a cloud bottom at the larger angles. Linear distance in space is scaled to radial position on the photograph by the arctangent function which means that far away objects are compressed drastically near the outer edge of the photo. Hazy conditions and thin cloud cover can also obscure cloud features. A red filter and a polarizer are being used to improve contrast and reduce glare. Color prints would help solve part of the problem but color photographs are considerably more expensive and difficult to develop.

C. Comparison of Fractional Cloud Cover Determination Methods

The fractional cloud cover values obtained by one method can be compared to values obtained by either of the other two methods to verify that each method is measuring the same thing. Comparisons to radiometric data will be discussed in the section on Correlation with Fractional Cloud Cover. Excellent agreement between the ground-based and satellite photometric results were obtained for the four test cases listed in Table IV. Since the satellite photoprints were used primarily to supplement ground based observations, only a small number of photoprints were obtained for this kind of test. The selected satellite-derived cloud fractions are underlined beneath the proper grid area heading in Table IV. The selection of single central grid results versus multiple grid area results is determined by overall cloud fraction and by cloud height. For the test cases only fairly

low, simple cumulus, clouds were visible in either the ground based photo or the satellite photo. This cloud height restricted the possible field of view on the ground to a smaller area than that represented by the 5x5 grid area on the satellite photo. More than fifty percent cloud cover further reduces the effective field of view since clear areas are hidden by clouds located between the camera and the clearings. This reduced area is only a small portion of the central satellite grid. Therefore for low level clouds and large fractional cloud cover, the 1x1 or central grid value is underlined. The 3x3 grid area is selected for smaller fractional cloud cover values. In general, the ground based photo results and satellite photo results agree well when the same region of sky is evaluated.

The distribution of clouds over a large region is generally ununiform and time dependent. Fractional cloud cover is also location and time dependent with appreciable changes occurring over distances of a few kilometers and over time intervals of a few minutes. The lack of uniformity in cloud fraction is observable in the April 24, 1981 data presented in Table IV by comparing the results for different size grid areas, since a shift of more than ten percent in each average indicates larger individual differences. This general behavior is also evident in any satellite photo with clouds present. This dependence on location introduces considerable uncertainty when two different widely separated sites are compared. However, a generally good correlation should exist between cloud cover measurements made at Langley Air Force Base (LAFB) and at Hampton Institute (HI) because the sky between the two is visible to both. The separation of the two sites is only about seven kilometers. Visual estimation of cloud cover is made regularly at LAFB every hour of the day by trained observers. Mr. Thomas Griffin, the Research Associate on this grant, has made a number of visual

cloud cover estimates at HI to accompany the ground-based photographs. He has had some formal training in the estimation of cloud cover while a graduate student at the University of Michigan. His visually estimated cloud cover fractions correlated well with the LAFB visual estimates and with both the satellite and ground-based photographic results as seen in Table V.

A graph of fractional cloud cover obtained from the 3x3 grid area on the satellite photoprints plotted against the visual cloud cover estimations made at HI is shown in Figure 11. A similiar plot for ground-based photograph results versus visual estimations at HI is shown in Figure 12. Comparisons of these cloud cover measurements were also made to LAFB visual estimates as shown in Figures 13 and 14. The same type of calculation was done for the single (1x1) and for the 5x5 grid area on the satellite photoprints. The linear regression coefficient and the number of data points are listed in Table V for each correlation. The best correlations were obtained for the 3x3 grid area for the satellite photoprint analysis method. The linear regression coefficients for the ground-based photographs and the satellite photoprint analysis methods have their largest values when correlated to the visual estimates made at HI. Many of the LAFB visual fractions used in the correlations are averages of the visual estimates at the beginning and at the end of each hour; whereas, all the HI visual estimates were made at the time of the photograph. Some averages of HI visual estimates were used in the correlation to the satellite-derived results since satellite photos are available only on the hour or half hour. The relatively low regression coefficients for the ground-based photographs is probably due to the much smaller field of view analyzed by this method.

The three different fractional cloud cover determination methods agree very well with one another when similar sky areas are analyzed. The best satellite photoprint analysis method developed was to estimate visually cloud

cover for each grid within a 5x5 grid area and average these fractions. Each grid represented a 24x24 km square on the ground. The inner 3x3 grid area corresponds well with the other measurement methods for short-time interval fractional cloud cover values. The full 5x5 grid should help time average as the clouds move about. Ground-based photograph results are valid for small sky area and short time intervals. This method is best used for small, widely scattered, low clouds that are hard to identify in a satellite photo because of satellite sensor resolution or low reflectivity of the clouds.

III. RADIOMETRIC AND METEOROLOGICAL DATA ANALYSIS

Continuous radiometric data collection commenced in February for global solar irradiance and in March for atmospheric emittance. An insufficient amount of diffuse solar irradiance data is available for significant analysis in this report. Meteorological data pertaining to clouds have been collected from the Third Weather Squadron at Langley Air Force Base (LAFB) for the months of March through June 1981. Fractional cloud cover data for this period have been obtained by the various methods discussed in the Fractional Cloud Cover Determination section of this report.

Average hourly values for global solar irradiance and atmospheric emittance (emitted infrared radiation) have been calculated for each hour of the day for each month of continuous operation. The average diurnal variation of global solar irradiance for the month of March is plotted in Figure 15. Average hourly global solar and atmospheric emitted irradiance are plotted together for the months of April, May, and June in Figures 16, 17, and 18, respectively. The decrease in average midday global irradiance from April to May is caused by a general increase in cloud cover during the 1000 to 1400 EST time period. If the cloud cover had remained unchanged, the midday global irradiance would have increased as the solar elevation at solar

noon increased from March through June.

The frequency of occurrence of certain sky cover fractions can be obtained from the LAFB observation data set. The number of times that each ten percent fractional cloud cover estimate was recorded during the month of March is plotted in Figure 19. All twenty-four hourly observations made each day are presented in the histogram. The distribution of cloud fractions is not uniform. Total cloud cover (100% cloud cover) is the most frequently reported value, and only about one-half of the observations fall in the partly cloudy (10-90% cloud cover) range. These sky cover fractions include transparent and semi-transparent clouds. Similar plots for other months, for restricted time periods, and for opaque cloud cover will be completed during the next month. Some opaque cloud cover results can be obtained from the LAFB data by careful observation of the cloud type codes.

IV. CORRELATIONS WITH FRACTIONAL CLOUD COVER

An empirical model developed by the Air Resources Laboratory (ARL) of the National Oceanic and Atmospheric Administration was selected for correlation of the global solar irradiance data with fractional cloud cover values. This is an established model used by many meteorological stations, and results are collected by the National Climatic Center in Asheville, North Carolina. The model is used to correlate hourly average global solar irradiance with opaque cloud cover which makes it particularly compatible with our solar energy and cloud cover measurement program. Another reason for selecting this model is that the results of this type of correlation for other measurement sites are readily available, and these results of the correlation can be used for comparison to other measurement sites in order to establish the uniqueness or representativeness of the measurement site at Hampton Institute.

The major factors that affect the amount of global solar energy received at the ground on a flat surface are solar zenith angle and opaque cloud cover. The ARL empirical equations selected for use with our measurements are:

$$(1)\quad SRC = A_0 + A_1 \cos ZA + A_2 \cos^2 ZA + A_3 \cos^3 ZA, \text{ and}$$

$$(2)\quad SR = B_0 + B_1\, OPQ + B_2\, OPQ^2 + B_3\, OPQ^3 + B_4\, RN.$$

SRC is the solar radiation hourly values for clear sky conditions and SR is the value for cloudy sky conditions. ZA is the zenith angle at the mid-point of each hour interval, and OPQ is the fractional opaque cloud cover. RN is a rain term that is equal to one if some form of precipitation is reported; otherwise it is zero. The coefficients for the first regression equation are calculated separately for mornings, and afternoons, for each month of the year in order to partially account for diurnal and seasonal changes in atmospheric turbidity, water vapor, and other such factors. The first and last partial hours of the day are not included in the regression calculation. The coefficients for the second equation are normally calculated for mornings, and for afternoons, using a full year of data at a time.

A. Clear Sky Results

The clear sky data have to be analyzed before the cloudy sky data can be normalized by its solar zenith angle dependence (time of day dependence). Determination of clear sky hours was made using the LAFB cloud observation data set. A plot of hourly values of the clear sky global solar for March mornings is shown in Figure 20(a). There were only ten full hours of clear sky in the mornings during the month of March. The line plotted through the data was obtained by the Marquardt's nonlinear least-squares method (Marquardt) using equation 1. The regression coefficients are listed in

Table VI. The results for the afternoon clear sky data are plotted in Figure 20(b) and are also listed in Table VI. The sign of A_0 in both regressions is negative but if the combined morning and afternoon data are used, the sign of A_0 becomes positive. Since A_0 is the "cos ZA" intercept in equation 1, it can be interpreted as being related to the clear sky global radiation value at sunrise or sunset when cos ZA becomes zero. This is outside the range of the fit to the data and causes A_0 to be sensitive to small changes in the data. Comparison of these coefficients must be made with great care. Analysis of a set of ARL coefficients (Kuhn) for various meteorological data sites does not indicate a significant pattern for the sign of the first coefficient. However, the term A_0 is much smaller in magnitude than A_1 or A_2 for all stations (usually only a few percent of A_1 or A_2).

Results for clear sky data for the month of April, and for mornings in May are presented in Table VI and in Figures 21 and 22. However, there were no clear hours in the afternoons for May and there were only five for April. The number of "clear" sky data points had to be increased in order to make the regression coefficients meaningful and to normalize the cloudy data for afternoons in May.

Analysis of the LAFB cloud observations produced a number of hours with small fractional cloud cover composed of cirrus or altocumulus clouds that were coded as being transparent, semitransparent, or "thin." The strip chart trace for each of these hours was examined. Global radiation values for these very thin cloud conditions were added to the clear sky data as long as the strip chart trace showed the smooth behavior characteristic of clear sky. The effect of clouds upon the global irradiance is evident in Figure 23 which is a copy of the PSP and PIR traces for April 27, 1981

for a wide range of fractional cloud cover. Regression coefficients with thin clouds present are listed in Table VI along with the total number of points used. In Figures 20 and 21, each clear sky data point is indicated by an "0" and the resultant least squares fit is drawn as a dashed curve. The data with thin clouds present scatter around the clear sky data rather well and extend the region of the fit to larger zenith angles. Note that the A_0 values for the morning and afternoon data for April and May have the proper magnitude relative to the A_1 and A_2 values. No thin cloud points were added to the March data, so the value for A_0 was obtained from only a few data points, a relatively large distance from the ninety degree point.

The coefficients A_1, A_2 and A_3 should be obtained from the results of the larger data sets for morning or afternoons over the three-month period. The ARL results for other sites (Kuhn) show that A_1 and A_2 are approximately equal and that A_3 is much smaller and negative. The preliminary results presented here suggest that A_2 is nearly 3 or 4 times as large as A_1, but the probable error in these coefficients does not rule out compatibility with the other radiometer data sites. The general magnitudes and signs are consistent.

B. Cloudy Sky Results

The cloudy sky to the clear sky global solar irradiance ratios were calculated for mornings and afternoons for each month. The regression coefficients for clear sky mornings, and for clear sky afternoons, were used in Equation 1 to estimate the clear sky irradiance for each hour interval. The cloudy sky data were then fitted to Equation 2 using the Marquardt's nonlinear least-squares method. Three sets of data for each month were generated by using the fractional cloud cover determined by satellite photoprint analysis, ground-based photograph analysis, and by LAFB visual esti-

mations. The LAFB observations were used to provide a common set of clear and totally cloudy points for each set since photos are not taken of clear or totally cloudy skies. Table VII lists the regression coefficients for each analysis. The data for March are plotted in Figure 24 with each satellite derived value denoted by an "o" and each ground-based photograph derived value denoted by a "+". There were only two ground-based photographs analyzed for the month of March since the photographic analysis and development procedures were just being completed. The linear regression for the LAFB visuals is indicated by the solid line and for the satellite data by the broken line.

The cloudy sky global irradiance divided by the clear sky global irradiance is plotted for April and May in Figures 25 and 26, respectively. The regression coefficients are listed in Table VII. The first coefficient, B_0, should be equal to one since it is the value of the cloudy to clear ratio at zero opaque cloud cover (clear sky). The last coefficient, B_4, is the average difference between the cloudy/clear ratios at 100% cloud cover with and without precipitation. This is because precipitation normally occurs for only totally cloudy conditions. The wide range in values for the other three coefficients does not allow a very meaningful analysis or comparison to published coefficients for other sites. All three graphs show considerable scatter in the cloudy/clear global fraction at cloud cover fractions greater than about ten percent. The corresponding scatter in fractional cloud cover values for a given ratio is very large, certainly more than the uncertainty in any of the cloud fractions. The spread is not explainable by the difference between the visual estimation site (LAFB) nd the radiometric site (HI) because the ground-based and satellite photographic results show the same amount of scatter.

The wide scatter in the data indicates that the global radiation is

not a simple function of fractional cloud cover and zenith angle. The strip chart trace for global solar irradiance on April 27, 1981, is shown in Figure 23. The large reduction in energy received for total cloud cover is evident by comparing the trace before 0800 EST to the clear sky trace after 1600 EST. The trace for a clear day is normally smooth and nearly symmetrical about solar noon (1203 EST). The effect of 60-80 % cloud cover can be observed between 1000 and 1600 EST that same day. The difference in the effect of partly-cloudy conditions seems to be primarily in the amount of time that the direct sun is obscured.

C. CONCLUSION AND SUMMARY

A major portion of the objectives of Phase I of the proposed three-year research project has been attained. The radiometric measurement program was completed for global solar and atmospheric emitted radiation. Direct and diffuse solar irradiance measurements will be in continuous operation as soon as permanent electrical power is made available. Fractional cloud cover can be routinely measured on a local scale by ground-based photographic techniques and on a larger scale by satellite photoprint analysis. A standard model has been selected for correlation between normalized global irradiance and fractional cloud cover. Cloudy sky global solar irradiance can be normalized by the expected clear sky values using the ARL model. Atmospheric emittance was not compared to fractional cloud cover because of the extremely weak dependence on cloud cover evident in the strip chart trace (see, for example, the trace shown in Figure 23). The regression coefficients, obtained by use of the ARL equations, are generally too indefinite and are valid for too short a time interval to provide meaningful analysis. The characteristics of the ground-based photographs have been established and can be used for measurements of cloud geometry in later phases of this project.

LIST OF TABLES

TABLE I

RADIOMETRIC INSTRUMENTATION AND WAVELENGTH CAPABILITIES

Instrument	Normal Observation Wavelength Range
Eppley Precision Spectral Pyranometer	0.285 to 2.8 microns
Eppley Precision Infrared Radiometer	4.0 to 50.0 microns
Eppley Normal Incidance Pyrheliometer	0.285 to 4.5 microns
Eppley Hickey-Frieden Absolute Cavity Pyrheliometer	0.2 to 50 microns
Additional Wavelength Ranges for the Pyranometers and Pyrheliometers	0.53 to 2.8 microns 0.63 to 2.8 microns 0.70 to 2.8 microns
Volz Sunphotometer	Center of Band - Halfwidth 380 nm - 11 nm 500 nm - 40 nm 875 nm - 17 nm 940 nm - 16 nm

TABLE II

HAMPTON INSTITUTE SOLAR MEASUREMENT SUMMARY

Measurement	Instrumentation	Data Frequency	Starting Date
SOLAR IRRADIANCES			
Global	Eppley PSP with clear glass	Continuous record on strip chart recorder	February 17, 1981
Direct	Eppley NIP with quartz glass and solar tracker	Integrated signals are printed at one hour intervals	September 1981
Diffuse	Eppley PSP with clear glass and occulting disk		September 1981
ATMOSPHERIC EMITTANCE	Eppley PIR	Continuous record on strip chart recorder Integrated signals are printed at one hour intervals	March 18, 1981
ATMOSPHERIC PROPERTIES			
Aerosol Extinction @ 380 and 875 nm Turbidity @ 500 nm Precipitable Water	Volz Sunphotometer	Approximately one hour intervals for clear sky	March 24, 1981

Figure 8. Analysis Grid for Ground-Based Whole Sky Photographs. Dotted circles represent half area ring segments. The light radial lines are half area sector lines. This overlay grid is centered over the photograph with the outside ring located at the edge of the photograph.

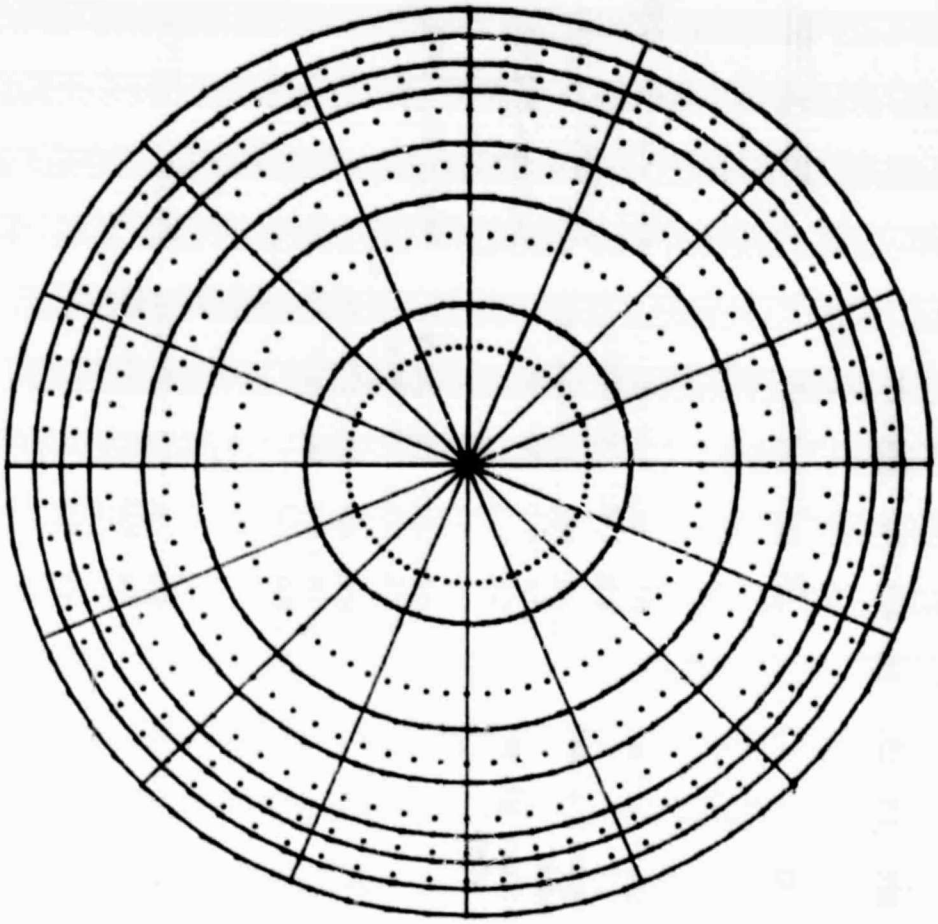

Table III RING POSITION AND WEIGHT FACTORS FOR THE GROUND-BASED PHOTOGRAPH ANALYSIS GRID

Ring #	Angle (degrees)	Δ Tan$^2\theta$	Weight Factor (with N=7)	Half Area Ring #	Angle (degrees)	Δ Tan^2 θ
1	30	0.333	0.003	1	22.2	0.167
2	50	1.087	0.008	2	43.1	0.543
3	60	1.580	0.012	3	56.1	0.790
4	70	4.549	0.035	4	66.5	2.274
5	75	6.380	0.049	5	73.0	3.190
6	80	18.235	0.140	6	78.2	9.118
7	85	98.483	0.754	(7)	83.7	49.242

TABLE IV COMPARISON OF FRACTIONAL CLOUD COVER OBTAINED FROM GROUND-BASED PHOTOGRAPH ANALYSIS WITH SATELLITE PHOTOPRINT ANALYSIS

Photo Date	Ground Based Photograph		Satellite Photoprint			
	Time (EST)	Fraction (per cent)	Time (EST)	Fractions (per cent) using the 1x1 - 3x3 - 5x5 grid areas		
Feb. 25, 1981	1355	57	1401	50	53	47
Mar. 3, 1981	0900	2	0901	0	3	5
Apr. 24, 1981	1441	60	1431	65	83	76
May 1, 1981	1328	22	1331	10	24	21

Selected satellite photoprint derived fractions are underlined. The 3x3 grid area is used for low fractional cloud cover and the single grid area is used for higher fractions as discussed in the text.

TABLE V REGRESSION COEFFICIENTS FOR FRACTIONAL CLOUD COVER METHOD COMPARISONS

Method Compared	Linear Regression Coefficients			
	No. of Points	LAFB Visual Estimates	No. of Points	HI Visual Estimates
HI Visuals	28	0.80	-	-
Ground Based Photos	19	0.66	18	0.79
Satellite Grid Areas				
1x1	29	0.75	14	0.79
3x3	29	0.88	14	0.92
5x5	29	0.84	14	0.88

TABLE VI ARL REGRESSION COEFFICIENTS FOR CLEAR SKY GLOBAL SOLAR IRRADIANCE

Data Correlated to Equation #1	Number of Points	Regression Coefficients (Wh/m^2) A_0	A_1	A_2	A_3
March - Mornings					
clear sky only	10	- 67	982	261	- 128
March - Afternoons					
clear sky only	14	- 52	1070	- 233	314
March - Mornings & Afternoons					
clear sky only	24	43	267	1568	- 911
April - Mornings					
clear sky only	8	- 248	1690	- 717	310
clear & thin clouds	19	- 29	758	578	- 267
April - Afternoons					
clear sky only	5	192	- 434	2648	-1426
clear & thin clouds	17	- 14	672	761	- 379
May - Mornings					
clear sky only	9	87	148	1181	- 434
clear & thin clouds	32	12	395	1108	- 533
May - Afternoons					
clear sky only	0	-	-	-	-
clear & thin clouds	12	48	166	1844	-1065
March, April & May - Mornings					
clear sky only	27	- 124	1173	- 44	- 174
clear & thin clouds	61	15	550	1440	- 838
March, April & May - Afternoons					
clear sky only	19	- 37	926	132	47
clear & thin clouds	58	9	489	1179	- 666

TABLE VII ARL REGRESSION COEFFICIENTS FOR CLOUDY SKY GLOBAL SOLAR IRRADIANCE

Month	Source of Fractional Cloud Cover Data	Number of Partly-Cloudy Fractions	Regression Coefficients B_0	B_1	B_2	B_3	B_4
March - (Base: 24 clear & 48 totally cloudy)							
	LAFB Visual Estimates	54	1.017	-0.282	-1.126	0.721	-0.168
	Satellite Photoprints	13	1.006	-0.735	0.851	-0.785	-0.175
	Ground-Based Photographs	2	-	-	-	-	-
April - (Base: 36 clear & 41 totally cloudy)							
	LAFB Visual Estimates	13	1.001	0.160	-1.493	0.620	-0.112
	Satellite Photoprints	9	1.001	0.328	-2.224	1.180	-0.110
	Ground-Based Photographs	12	1.003	-0.238	-0.469	-0.001	-0.121
May - (Base: 44 clear & 83 totally cloudy)							
	LAFB Visual Estimates	35	1.006	-0.499	-0.523	-.370	-0.184
	Satellite Photoprints	16	1.005	-0.411	-0.465	0.222	-0.180
	Ground-Based Photographs	10	1.004	-1.645	3.573	-2.581	-0.181

LIST OF FIGURES

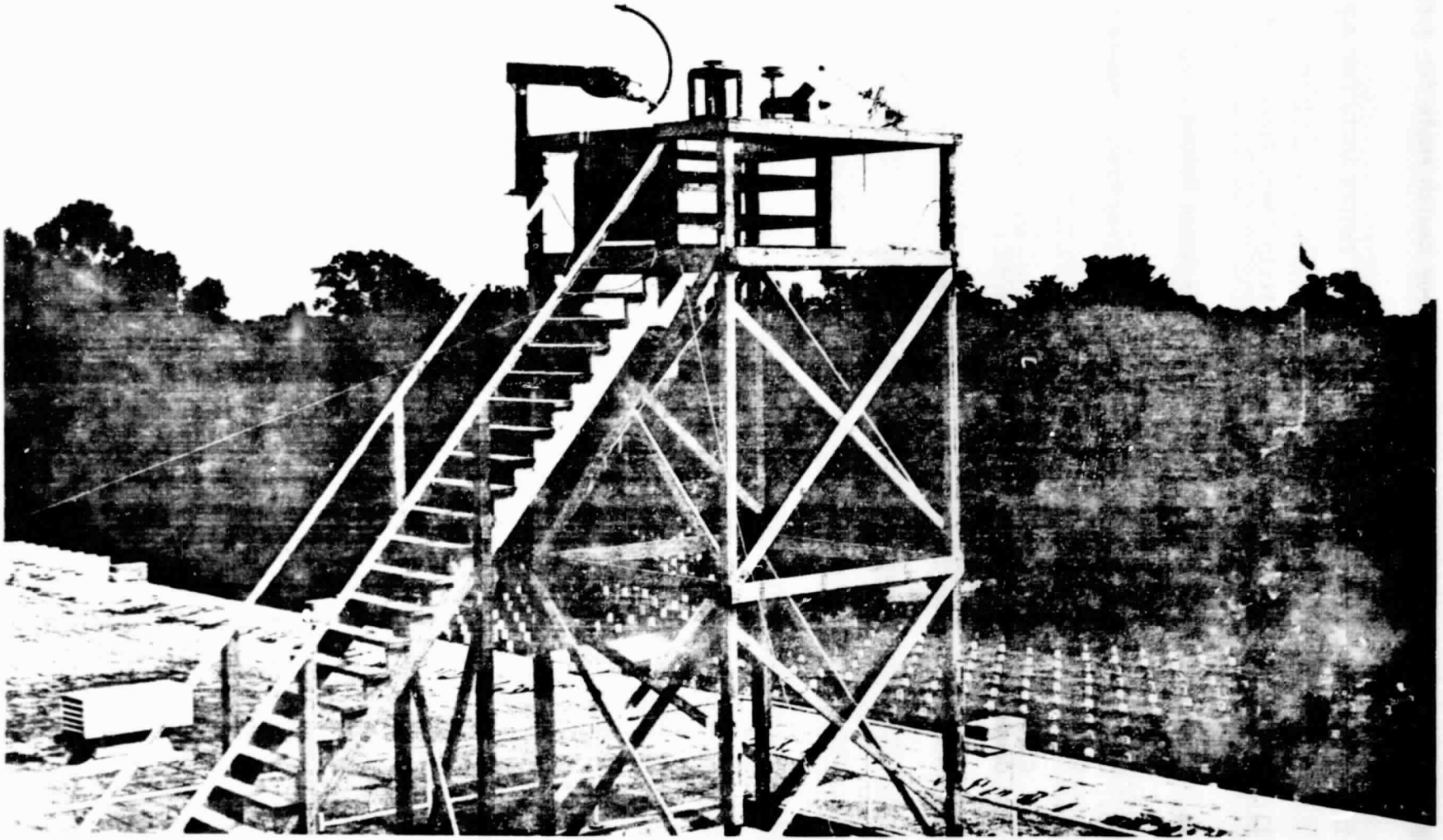

Figure 1. Solar Radiation Measurement Observation Tower. The instrumentation from left to right are: Diffuse Solar Tracker and Eppley PSP, Eppley PIR, Eppley PSP, Camera mount and occulting ball, and the Eppley NIP mounted on a Solar Tracker.

Figure 2. Occulting Disk-Solar Tracker Assembly

The disk at the upper right shades the sensor of the Eppley PSP from the direct sun. The motor assembly rotates the disk support arm to allow continuous operation from sunrise to sunset.

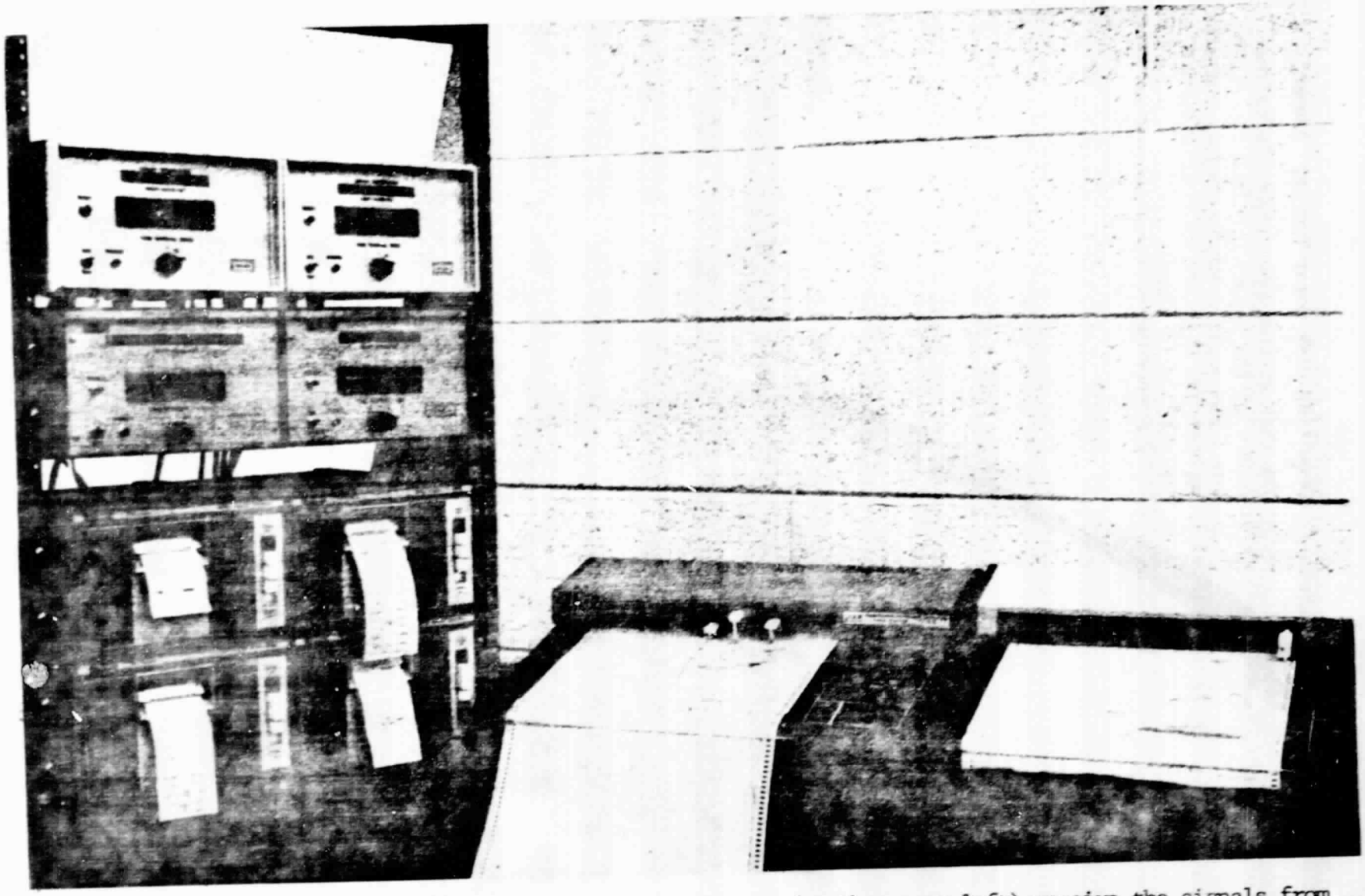

Figure 3. Data Acquisition System. The Eppley integrators (at the upper left) receive the signals from the radiometers on the observation tower. These signals are amplified and then displayed on the strip chart recorders at the right. Integrated signals are displayed on the LED readout and sent to the Digitec Printers (lower left) once an hour for printing.

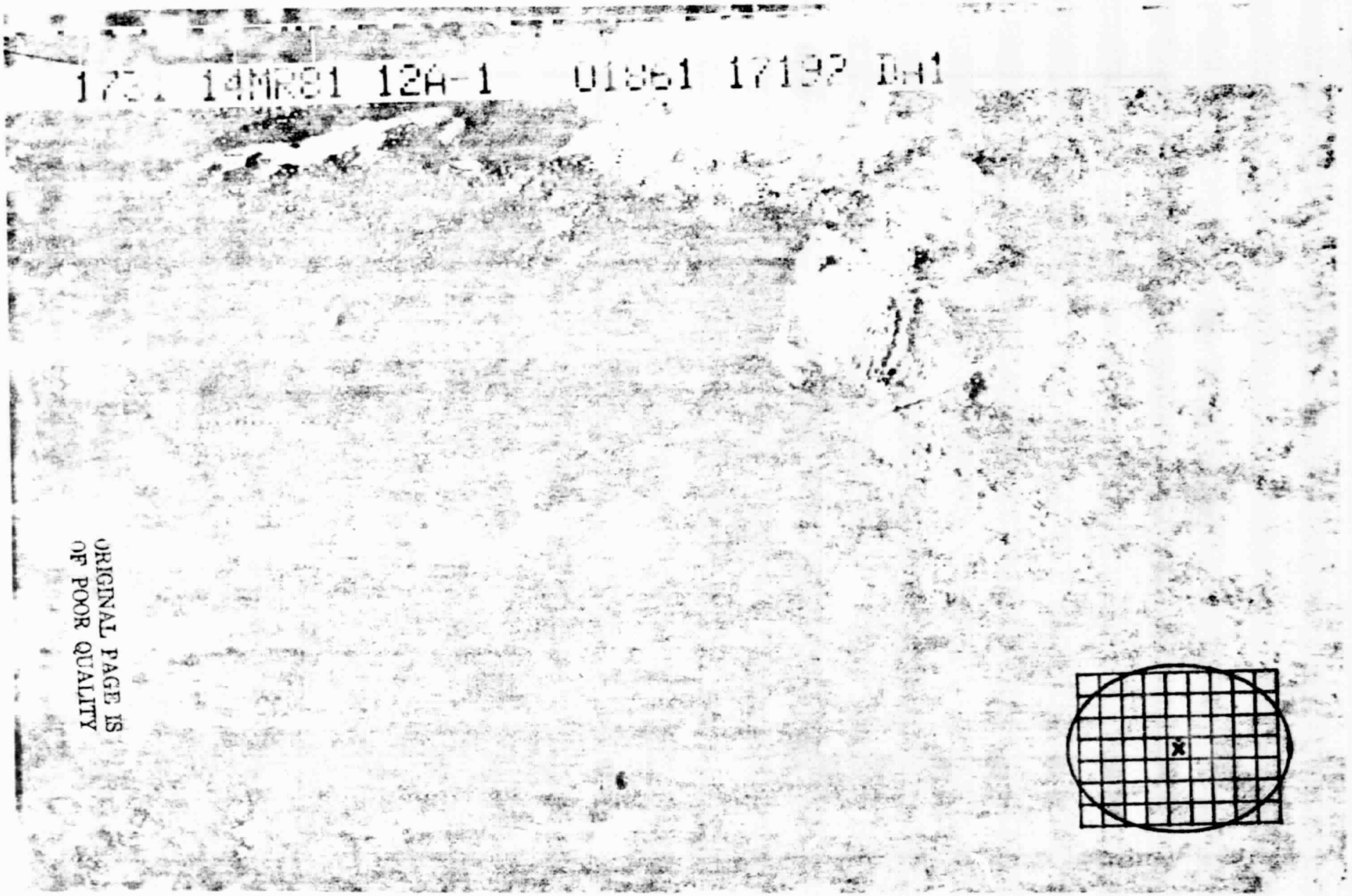

Figure 4. Copy of GOES - East, Sector DA-1, 14, March 1981, 1731 GMT 10"x10" visible spectrum photoprint. Horizon grid represents a 240 km diameter circle on the ground centered at Hampton Institute. Each square grid represents a 32 km x 24 km rectangular space on the ground. The relative positions of Hampton Institute and Langley Air Force Base are indicated by the X and the dot, respectively.

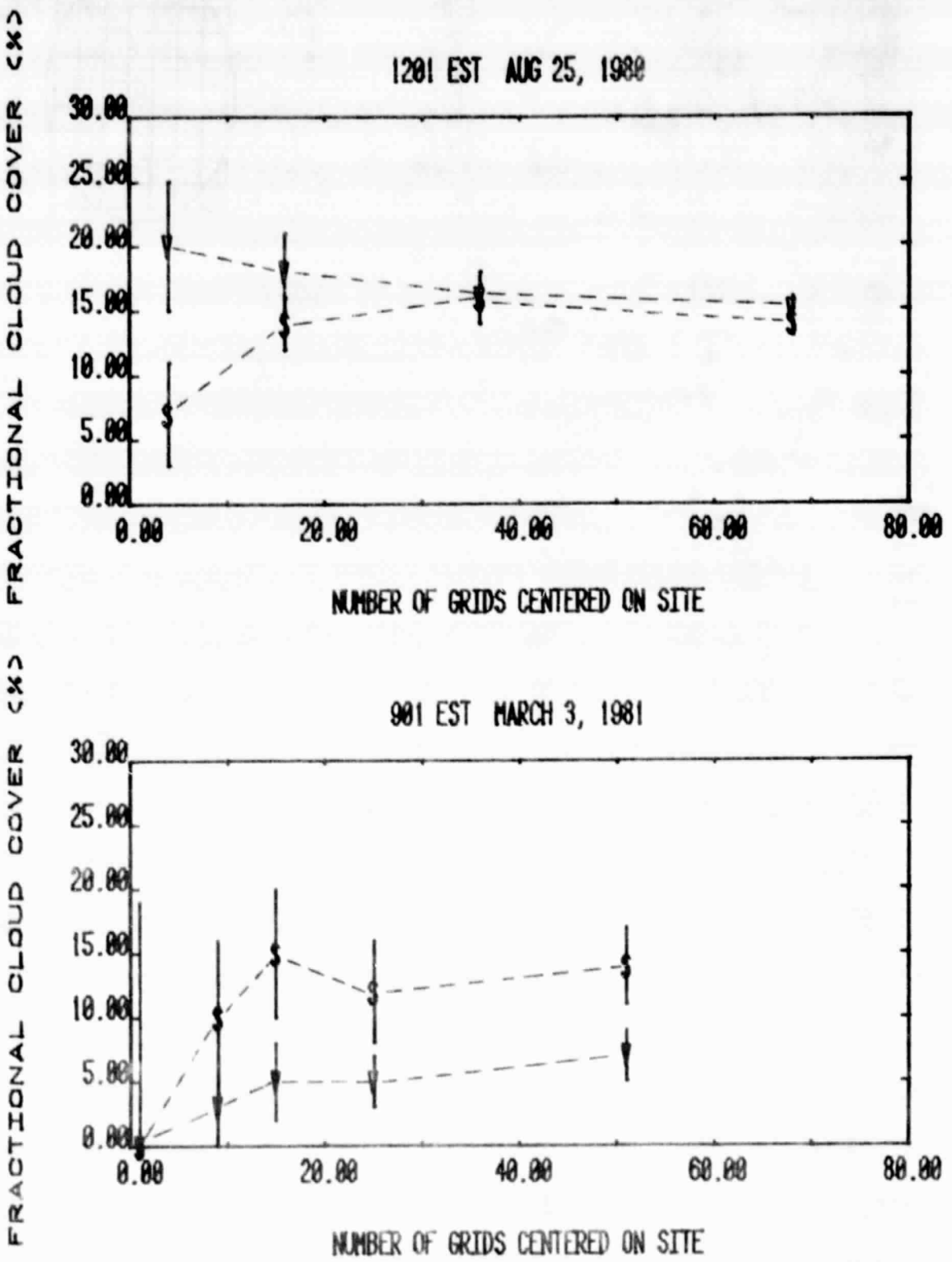

Figure 5. Reflection Densitometer versus Visual Estimation Analysis Methods for Two Selected Satellite Photoprints. The symbol "V" is used for visually estimated fractions and "S" is used for densitometric values. The error bars only account for statistical fluctuations.

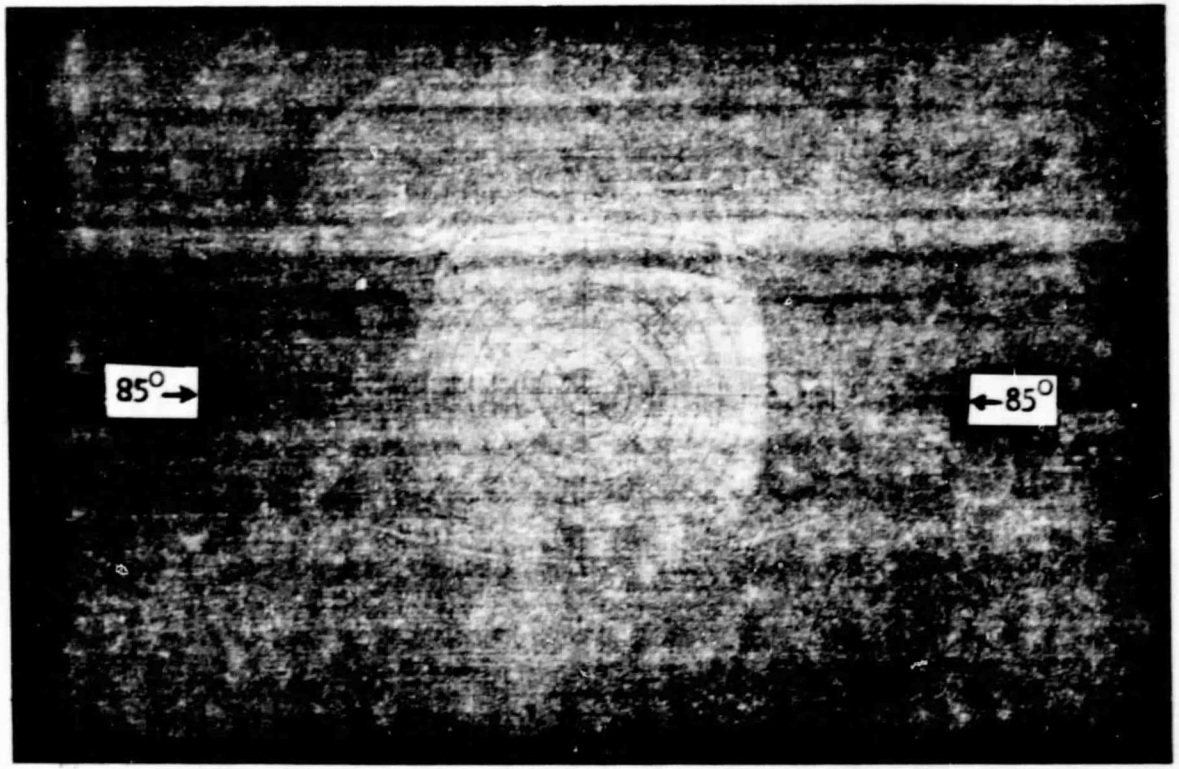

Figure 6. Copy of the First Fisheye Calibration Photo. The circles represent angles below 40° in 5° intervals. The plus marks on this classroom wall represent larger angles. The arrows at the left hand and right hand edges of the photo point to the 85° illuminated spots. This photo was taken with a Ricoh XR-2 35 mm SLR camera with an Aetna fisheye adaptor lens located 10.5" from the wall. Camera settings were: film speed @ 125 ASA, 50 mm lens @ f/2 and fisheye lens @ f/5.6, automatic shutter speed, focal distance set at infinity.

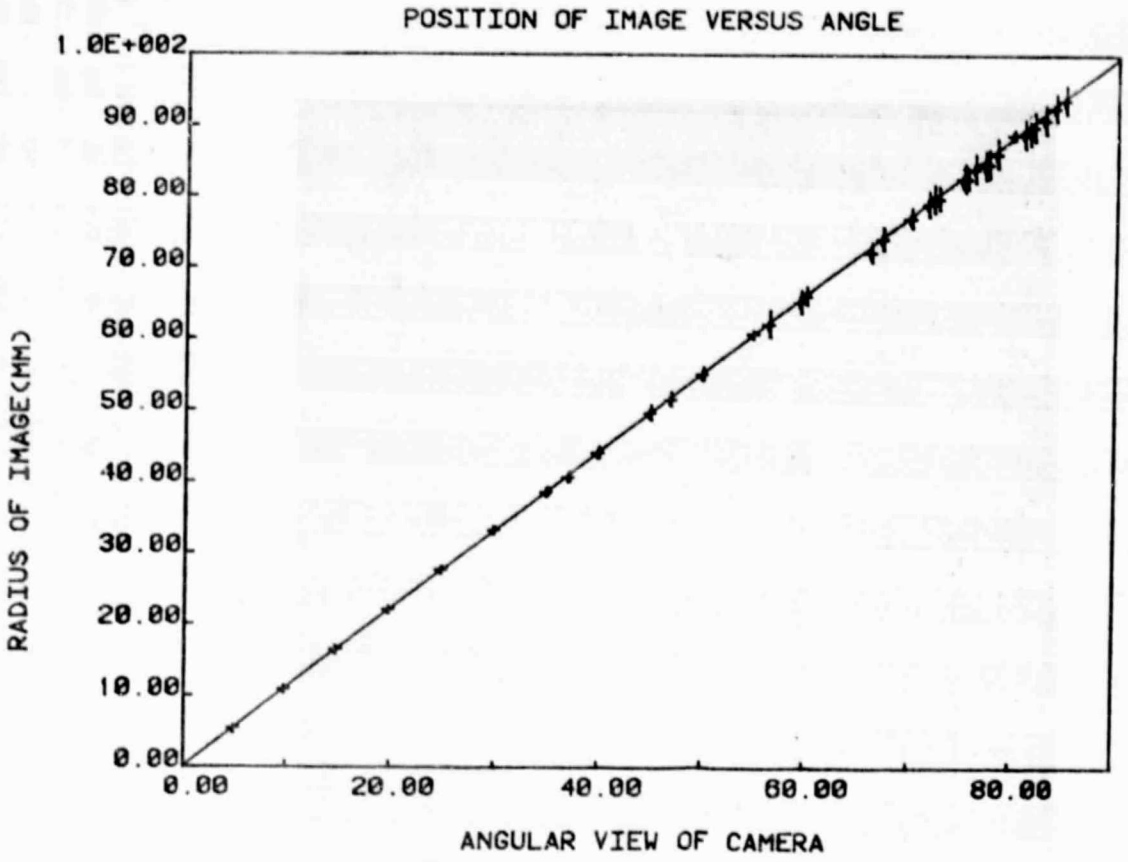

Figure 7. Results of the Whole Sky Photographic System Calibration. The distance of the image from the center of the photo is plotted versus the angular position of the object as measured from the principal axis of the lens system. The error bars represent the standard deviations of the data for the different orientations on the two calibration photographs.

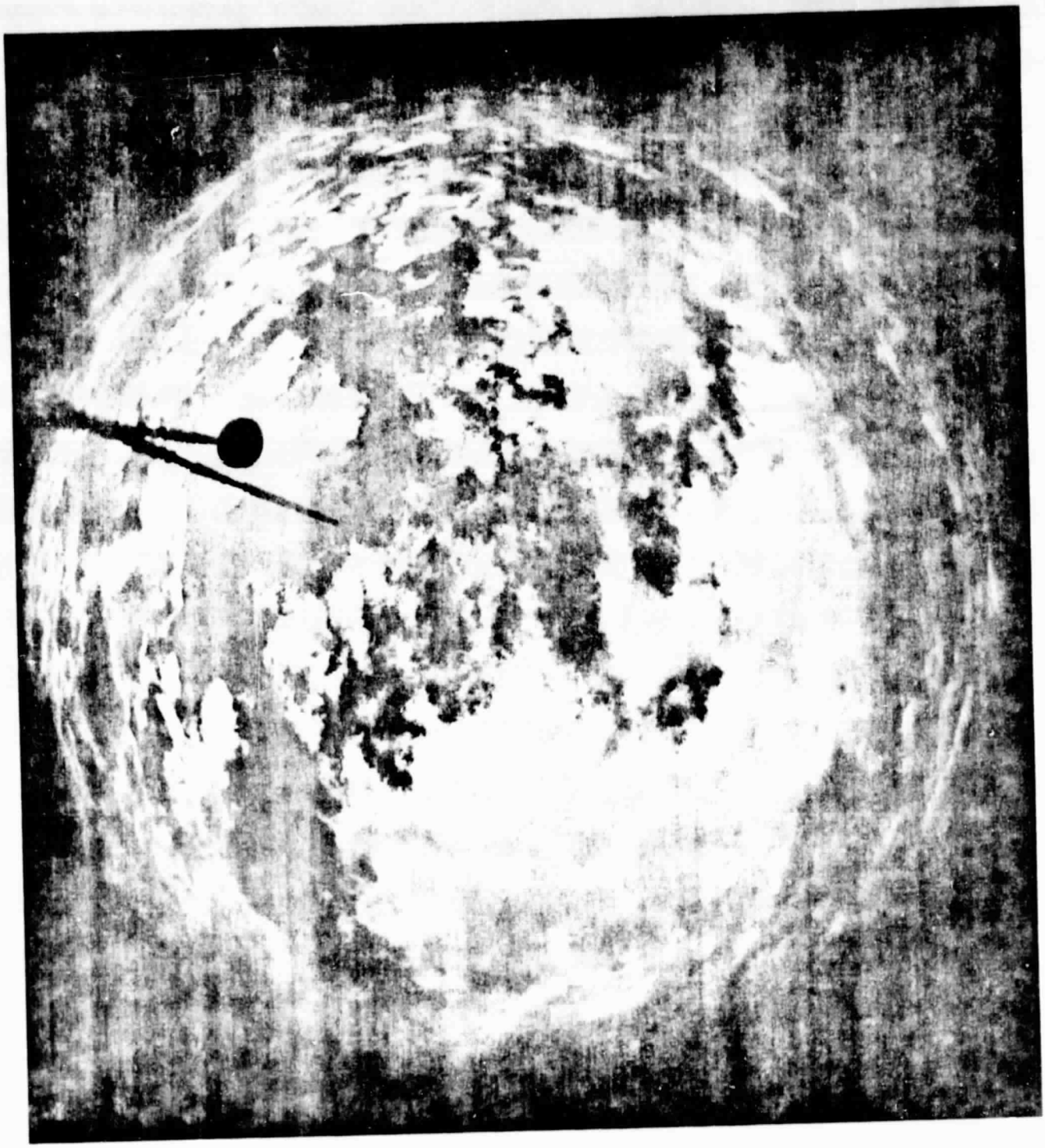

Figure 9. Copy of the 1350 EST Photo Taken February 25, 1981. The occulting ball and support rod are clearly visible in the photo. The ball is slightly west of due south with respect to the center of the photo. The measured cloud fraction is 59 %.

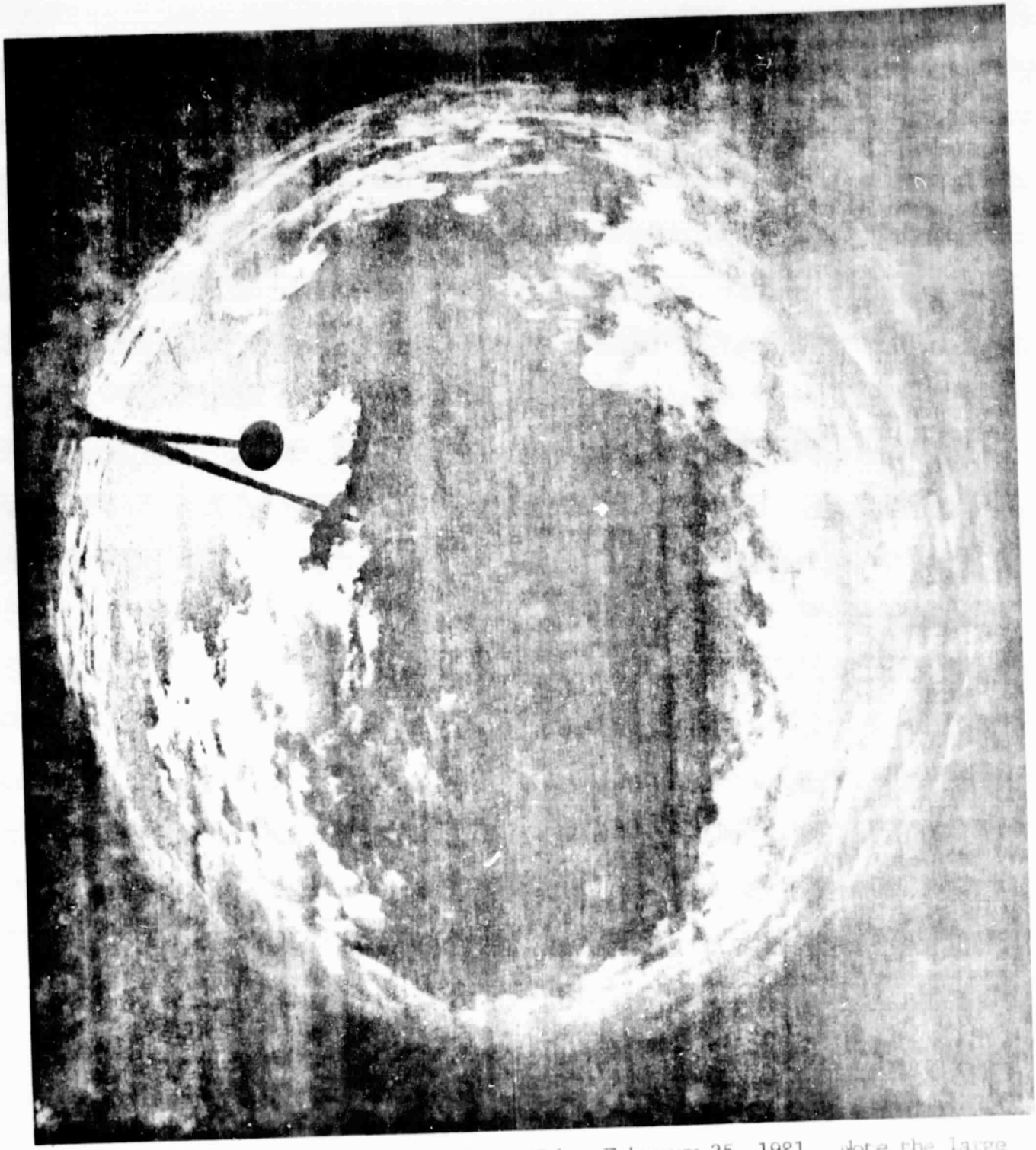

Figure 10. Copy of the 1355 EST Photo Taken February 25, 1981. Note the large clear region near the center of the photo. The measured cloud fraction was 57 %. The smoke stack is barely visible in the photo above the occulting ball. The smoke stack has an elevation of 7.5° above the horizon.

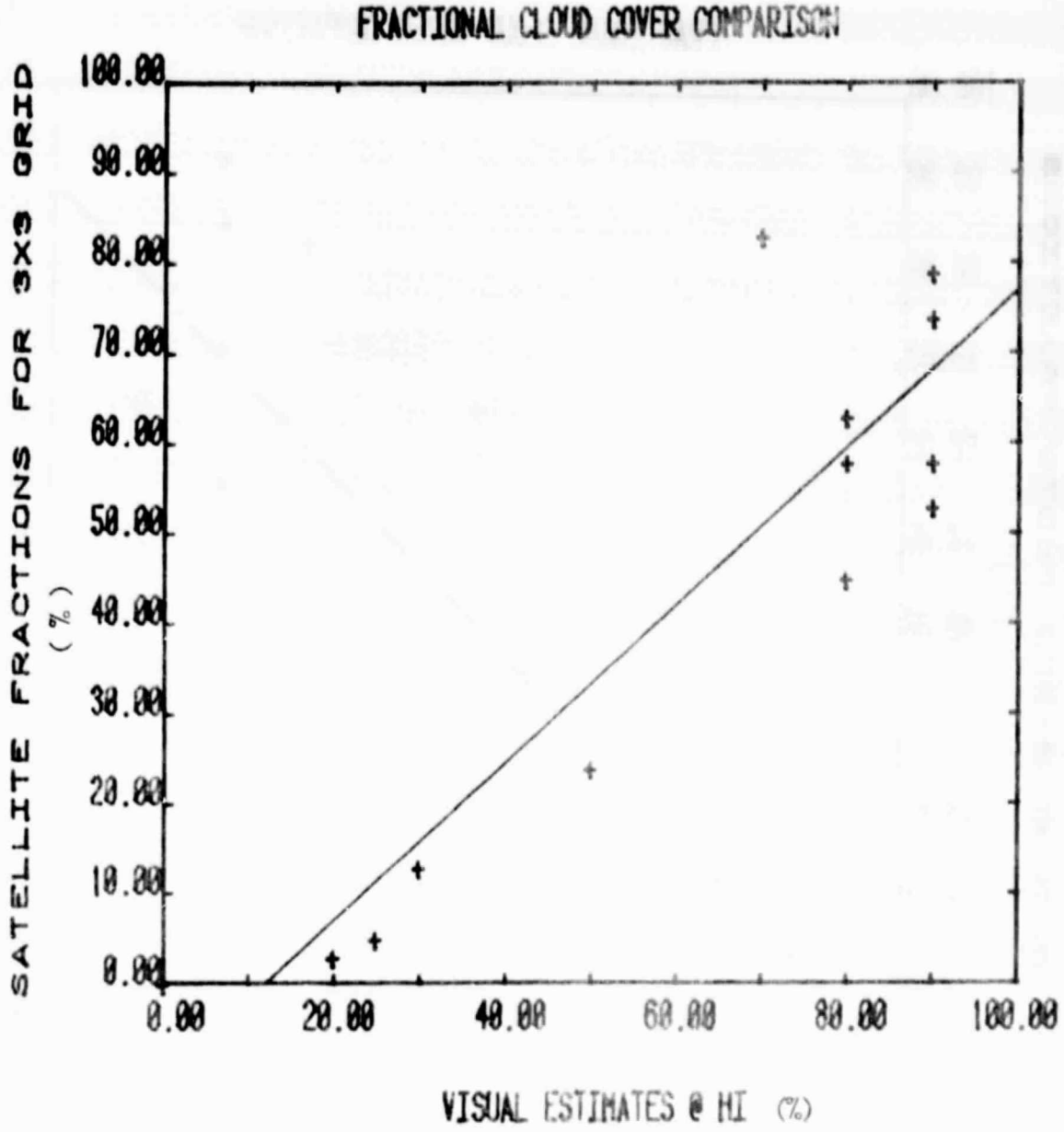

Figure 11 Fractional Cloud Cover Comparison between Satellite Photoprint Analysis Values and Ground Based Visual Estimates Made at Hampton Institute. The satellite data were calculated using the nine rectangular grids (3x3) centered over the measurement site. Cloud Cover was estimated for each grid and then averaged.

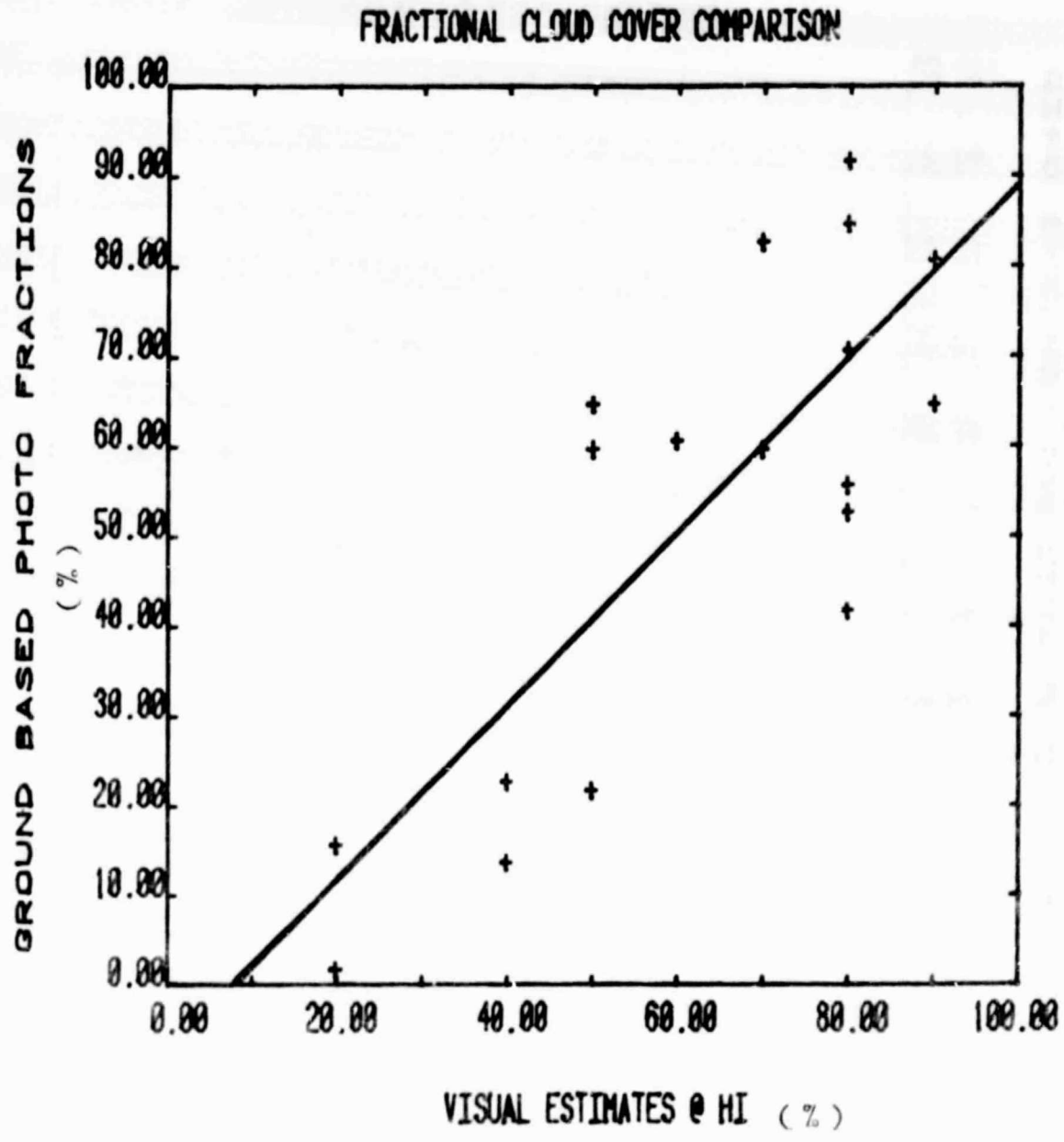

Figure 12. Fractional Cloud Cover Comparison between Ground Based Photographic Results and Ground Based Visual Estimates Made at Hampton Institute. The first five rings (up to 75^{0}) were used for the ground based photographic results.

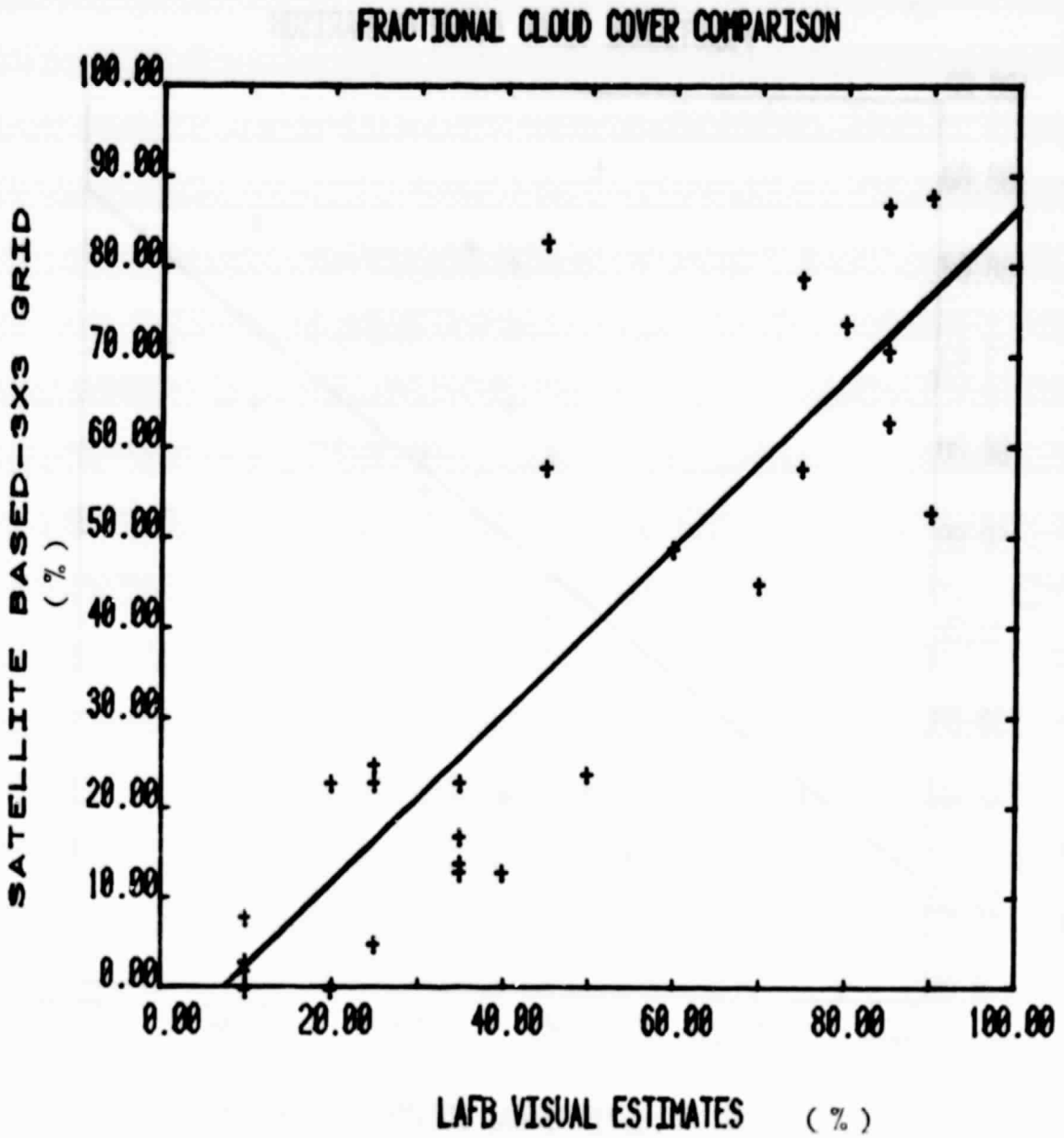

Figure 13. Fractional Cloud Cover Comparison between Satellite Photoprint Analysis Values and Ground Based Visual Estimates Made at Langley Air Force Base. The satellite data were calculated using the nine rectangular grids (3x3) centered over the measurement site. Cloud Cover was estimated for each grid and then averaged.

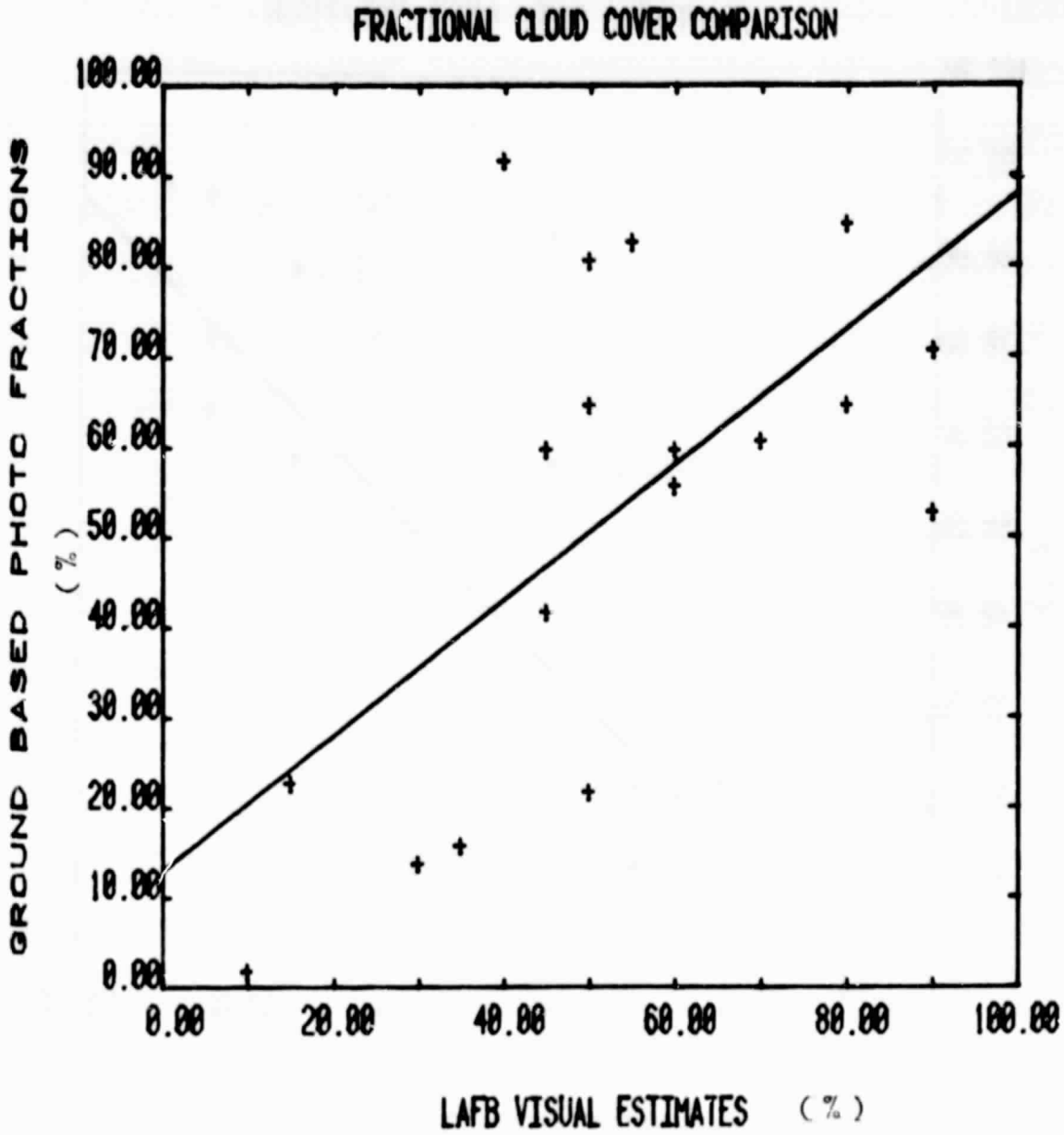

Figure 14. Fractional Cloud Cover Comparisons between Ground Based Photographic Results and Ground Based Visual Estimates Made at Langley Air Force Base. The first five rings (up to 75°) were used for the ground based photographic results.

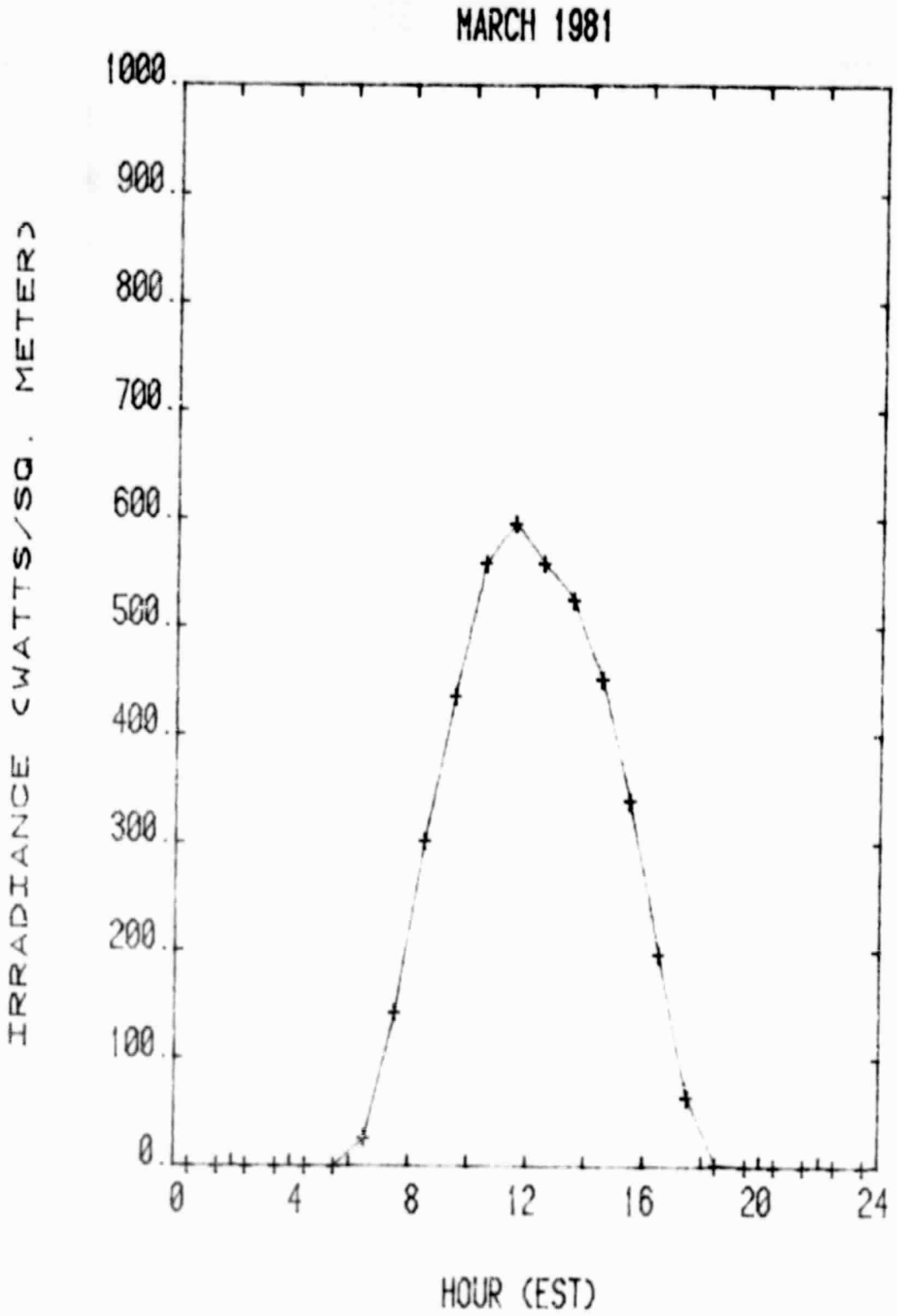

Figure 15. Average Diurnal Variation of Global Solar Irradiance for March 1981. The average global solar irradiance incident on a horizontal surface for each hour of the day is plotted versus the time of day for the month of March 1981.

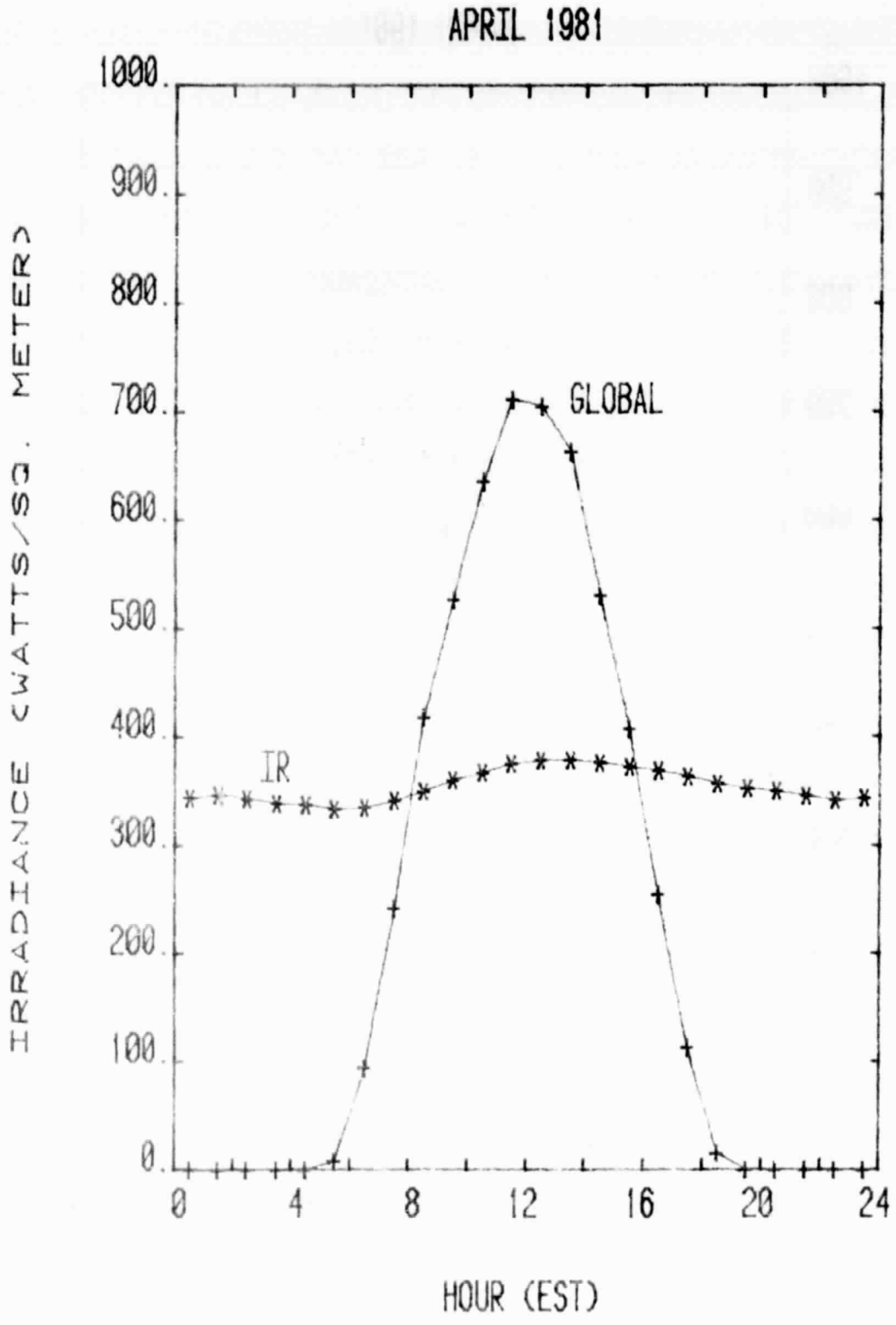

Figure 15. Average Diurnal Variation of Global Solar Irradiance and Atmospheric Emittance for April 1981. The average global and atmospheric (IR) radiation received on a horizontal surface for each hour of the day is plotted versus the time of day for the month of April.

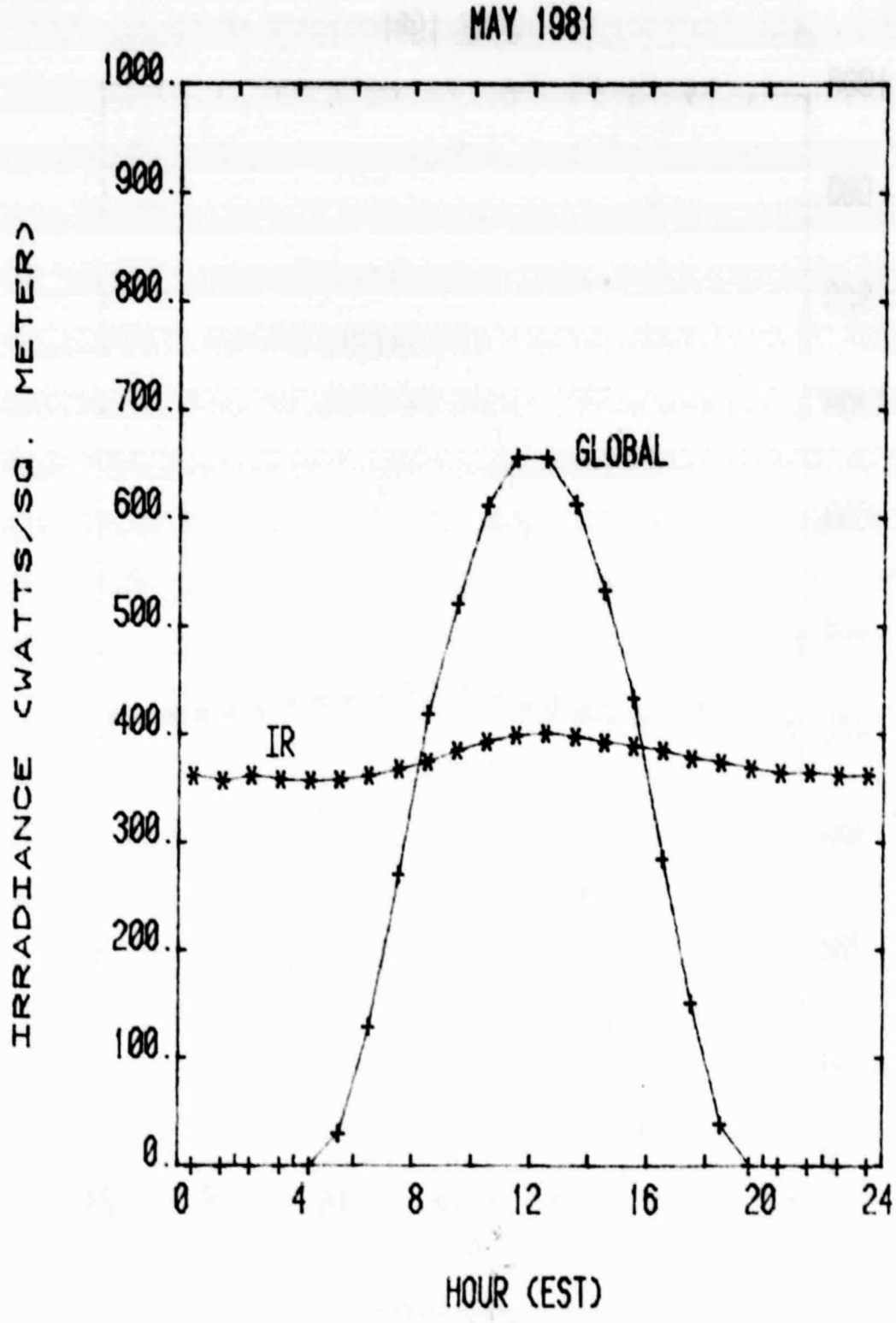

Figure 17. Average Diurnal Variation of Global Solar Irradiance and Atmospheric (Emittance for May 1981. The average global and atmospheric radiation received on a horizontal surface for each hour of the day is plotted versus the time of day for the month of May.

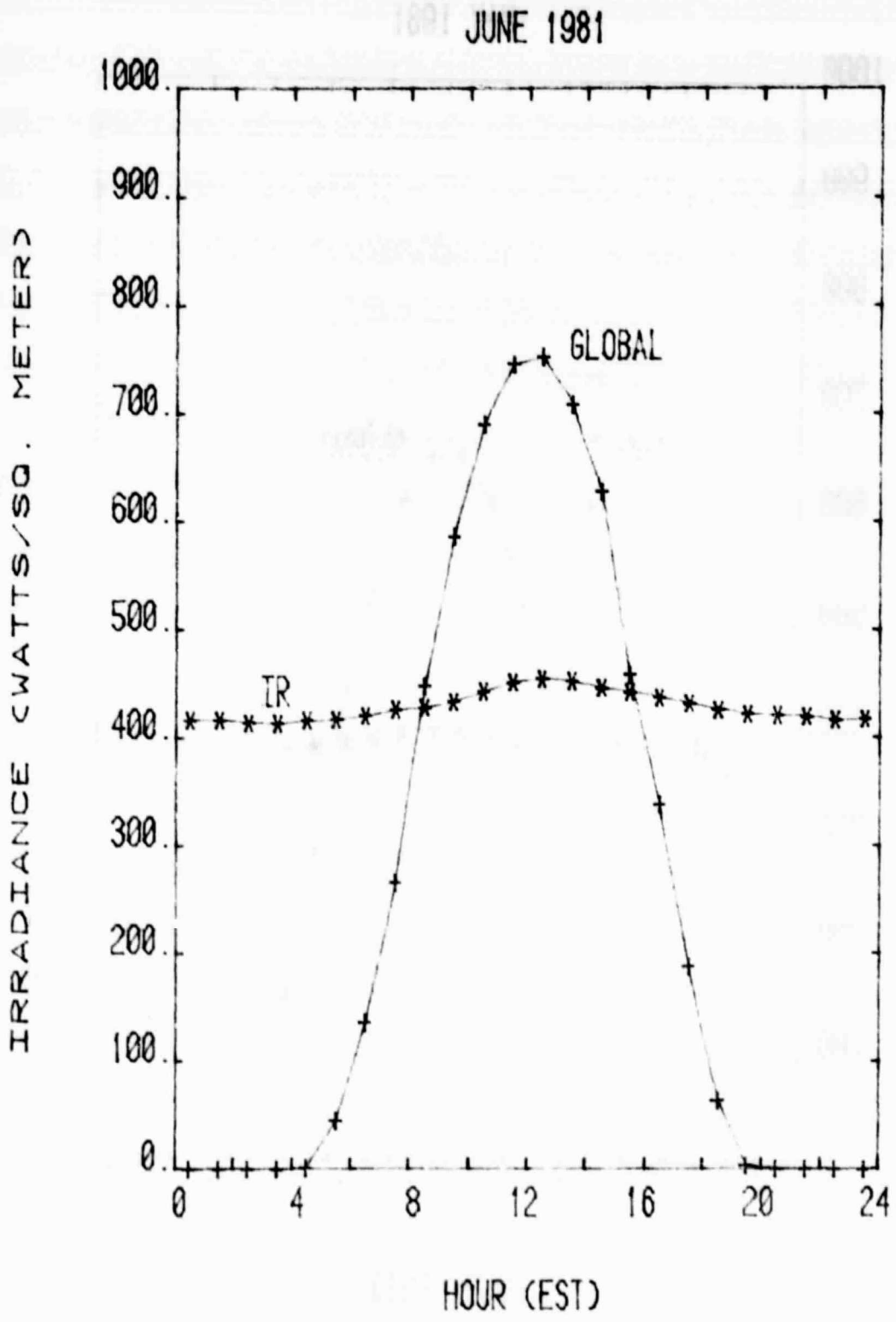

Figure 18. Average Diurnal Variation of Global Solar Irradiance and Atmospheric (IR) Emittance for June 1981. The average global and atmospheric radiation received on a horizontal surface for each hour of the day is plotted versus the time of day for the month of June.

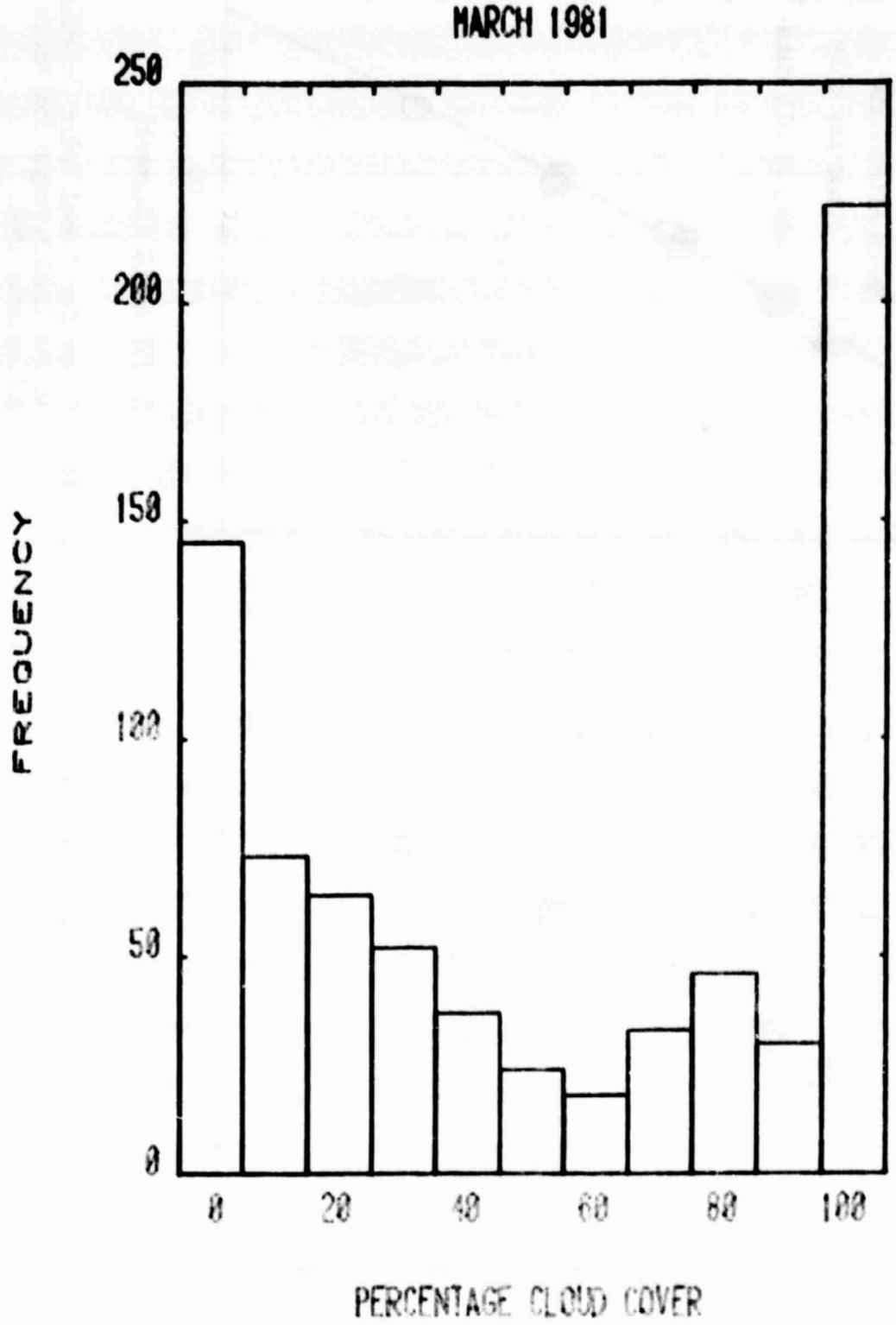

Figure 19 Fractional Cloud Cover Frequency for March 1981. The total number of times that each ten per cent cloud cover estimate was made during the month of March is plotted versus fractional cloud cover. The graph reflects each hourly observation made during the 24 hour day for all 31 days. The cloud observations were provided by the Third Weather Squadron at Langley Air Force Base.

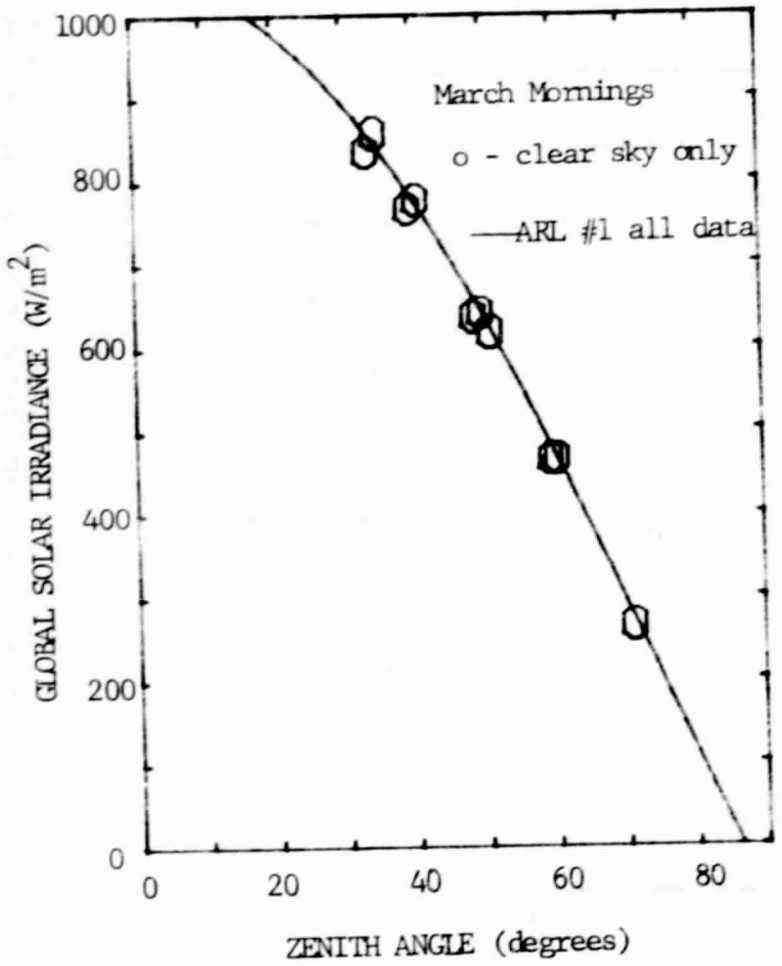

Figure 20(a). Clear Sky Global Solar Irradiance versus Zenith Angle for March Mornings 1981.

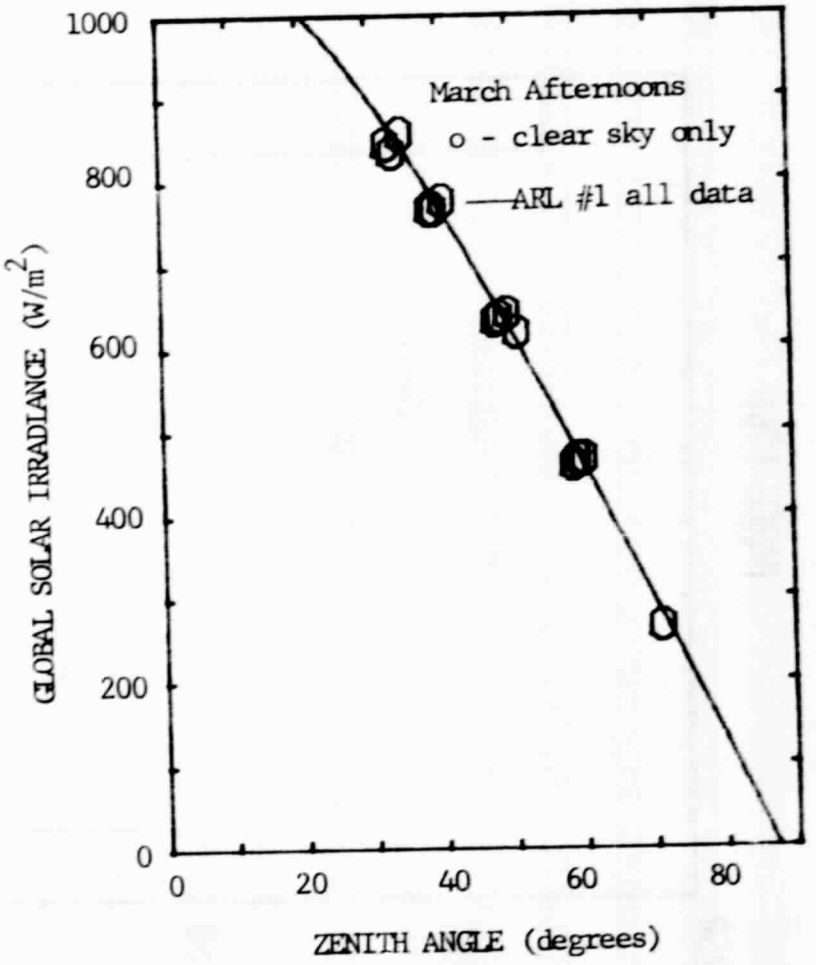

Figure 20(b). Clear Sky Global Solar Irradiance versus Zenith Angle for March Afternoons 1981.

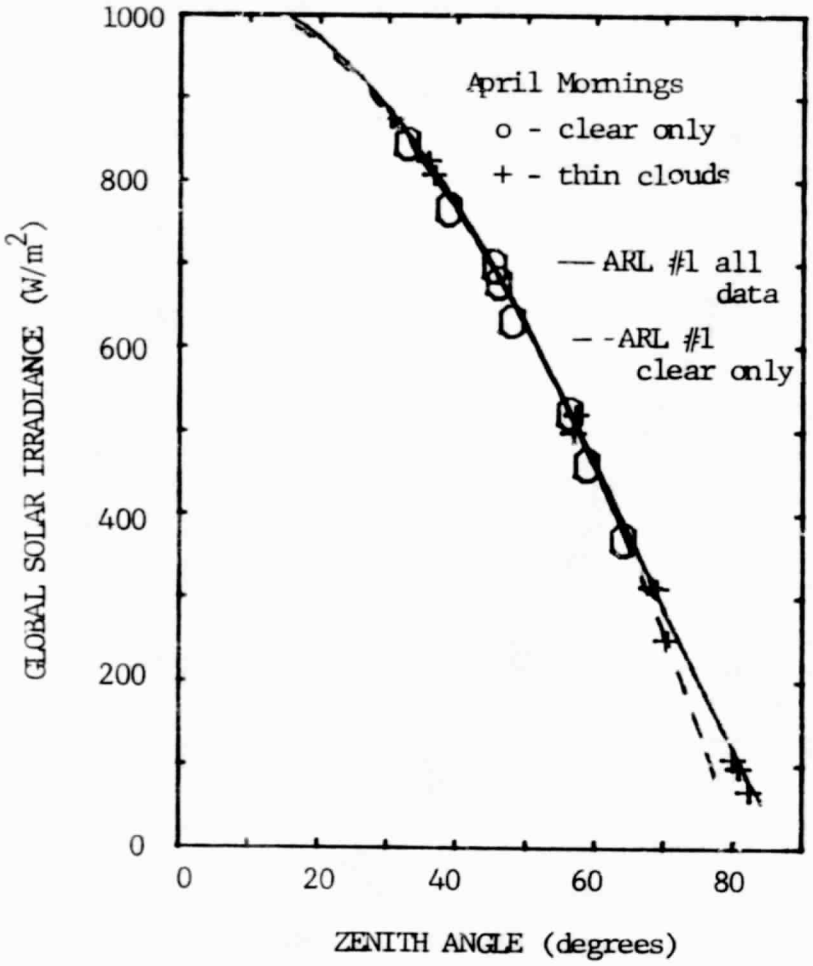

Figure 21 (a) Clear Sky Global Solar Irradiance versus Zenith Angle for April Mornings 1981. Thin cloud data are included in the graph.

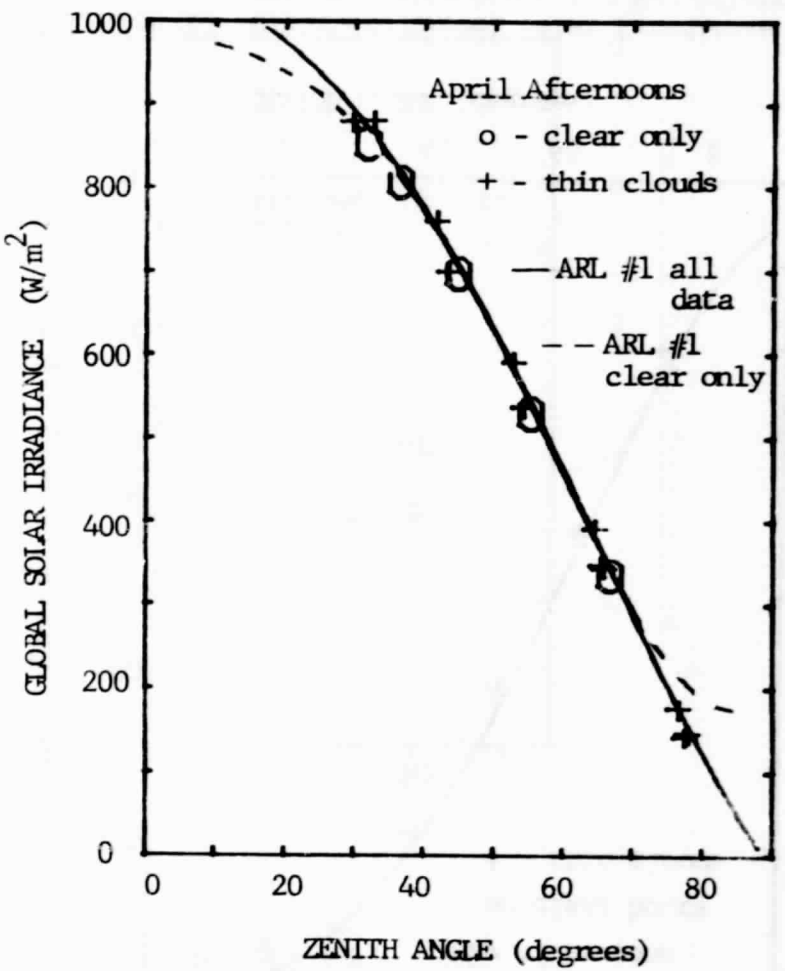

Figure 21 (b). Clear Sky Global Solar Irradiance versus Zenith Angle for April Afternoons 1981. Thin cloud data are included in the graph.

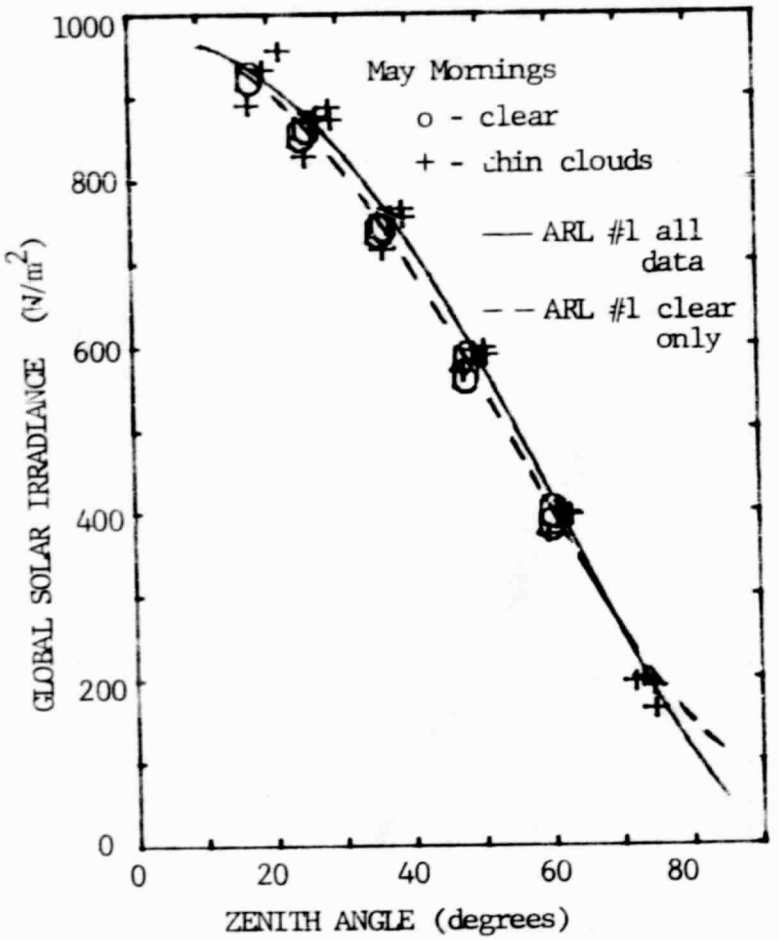

Figure 22 (a) Clear Sky Global Solar Irradiance versus Zenith Angle for May Mornings 1981. Thin cloud data are included in the analysis.

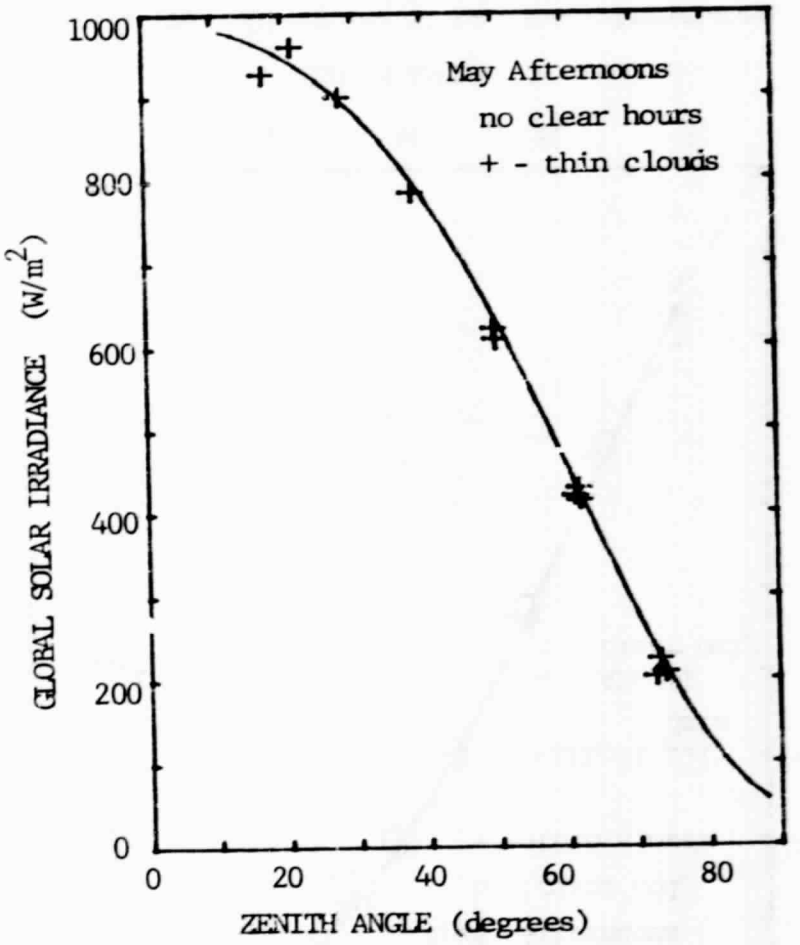

Figure 22 (b) Clear Sky Global Solar Irradiance versus Zenith Angle for May Afternoons 1981. Thin cloud data are the only data available for analysis.

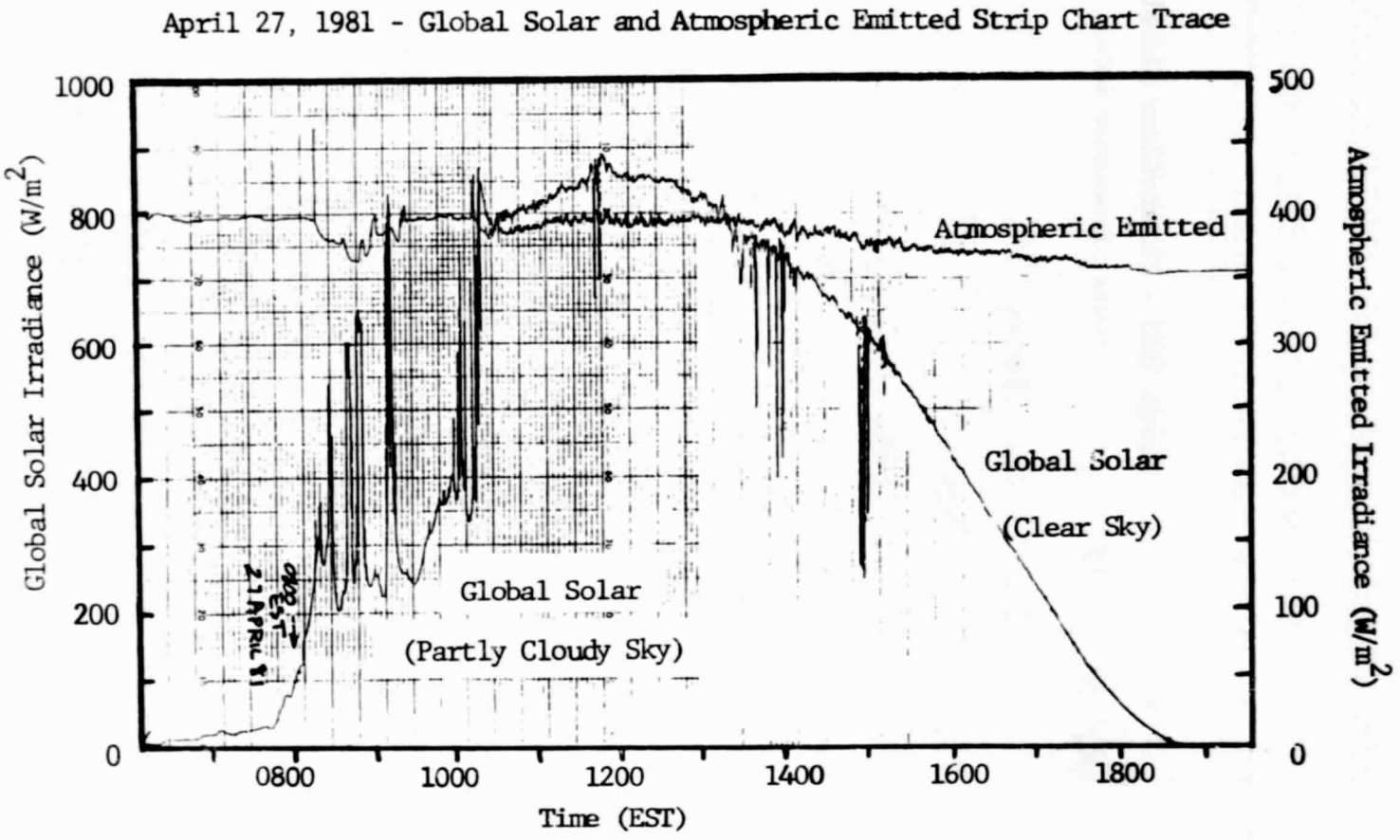

Figure 23. Global Solar and Atmospheric Emitted Strip Chart Trace for April 27, 1981.

The relatively low values of the global trace before 0800 EST are caused by the presence of total cloud cover. From 0800 to 1000 EST the cloud fraction varied between 100 % and 60 % with 61% measured at 0901 EST by a ground-based photograph. The predominant cloud type was cumulus with some altocumulus and cirrus present. After 1000 EST the fractional cloud cover decreased sharply to around 30% cumulus and cleared up completely just before 1600 EST. The very smooth global trace after 1600 EST is indicative of clear sky. The atmospheric emittance trace does not show a strong dependence upon the fractional cloud cover.

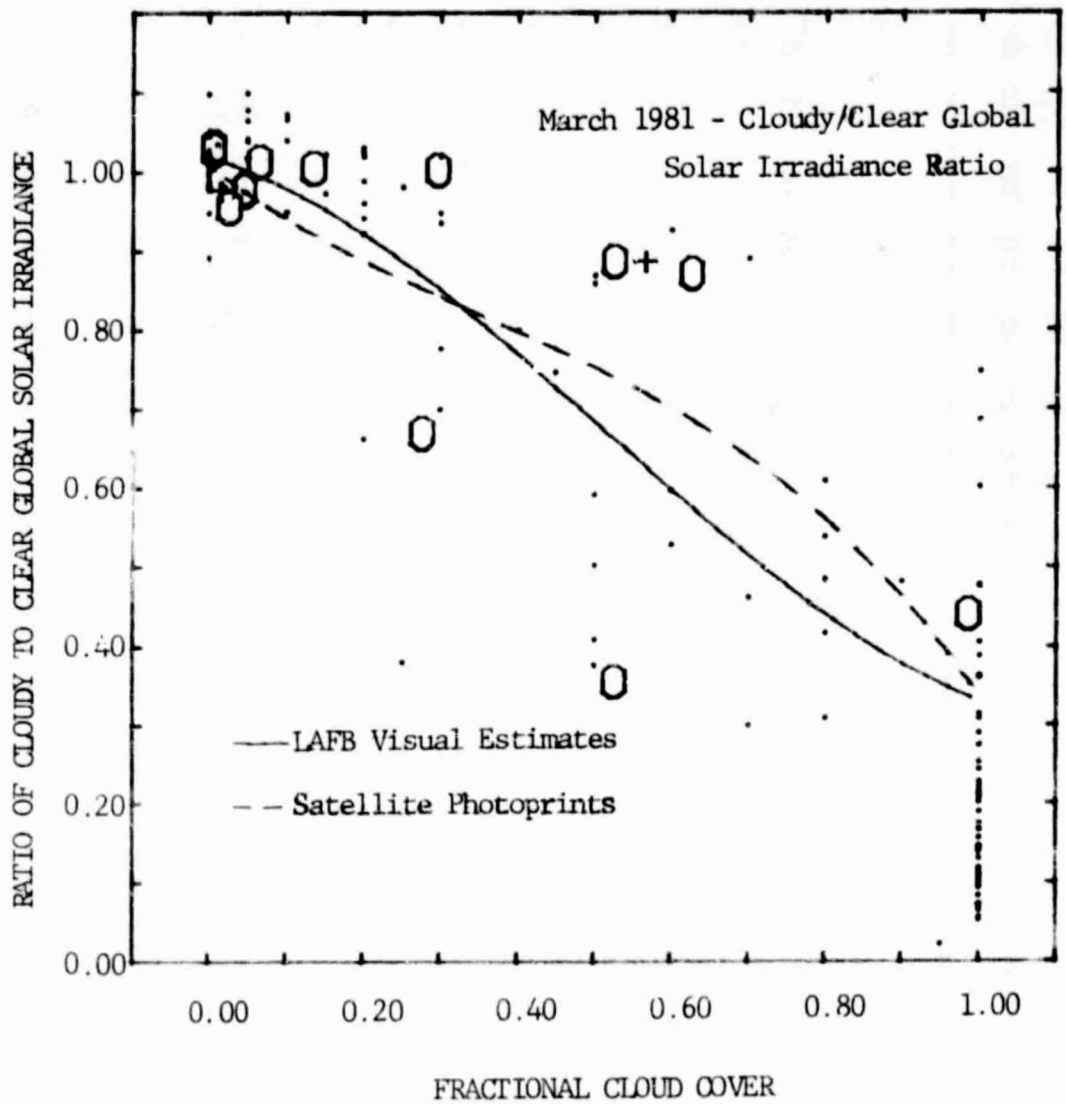

Figure 24. Cloudy to Clear Global Solar Irradiance Ratio versus Opaque Cloud Cover for the Month of March. The dots represent LAFB cloud fractions and each O represents a satellite-derived cloud cover fraction. The two plus marks designate ground-based photograph derived fractions. The solid line is the result of the least squares fit to the LAFB visual estimates using equation 2. The broken line is for the satellite photoprint derived fractions.

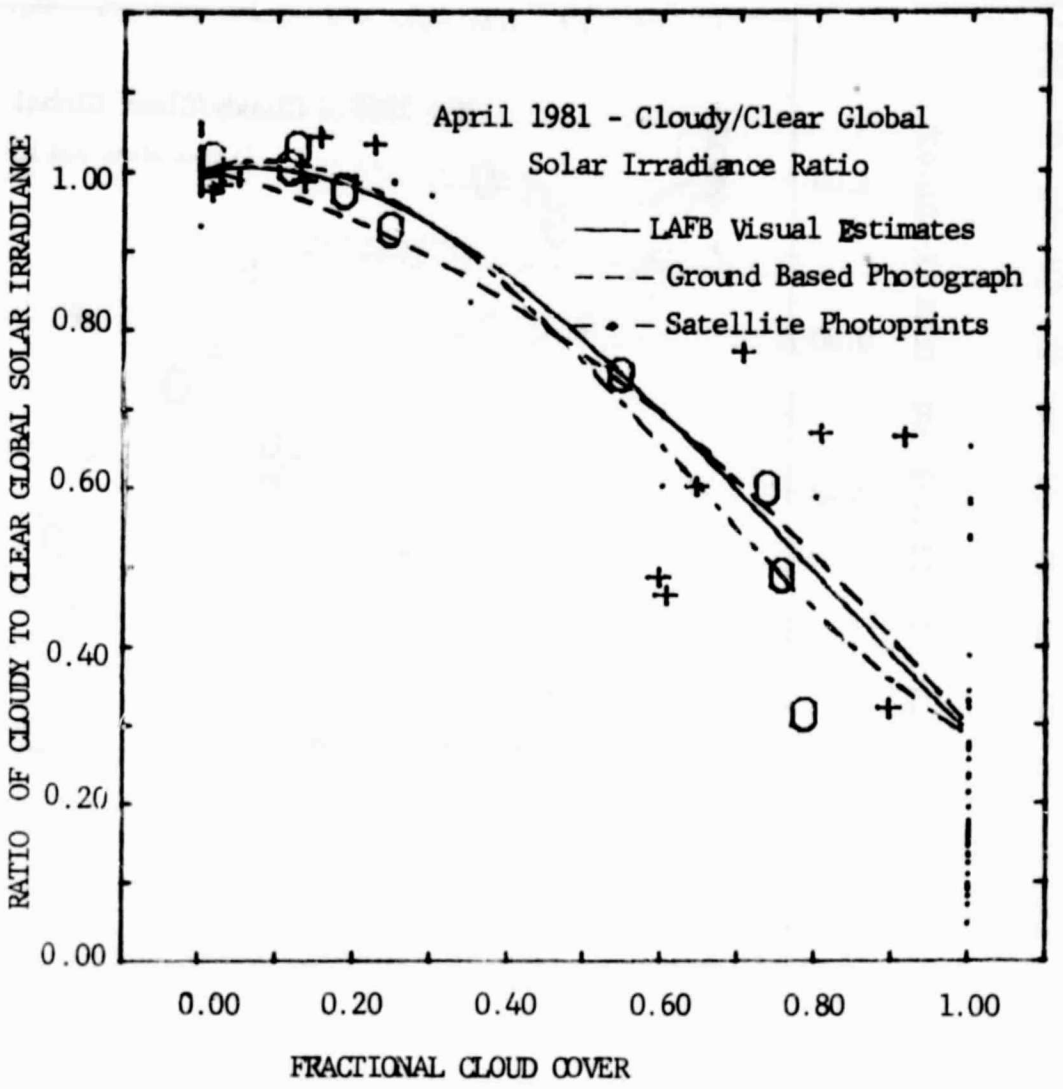

Figure 25. Cloudy to Clear Global Solar Irradiance Ratio versus Opaque Cloud Cover for the Month of April 1981. The dots represent the LAFB cloud cover fractions and each O represents a satellite-derived cloud cover fraction. Each + designates ground-based photograph derived fractions. The solid line is the result of the least squares fit to the LAFB visual estimates using equation 2. The dashed line is for the ground-based photograph results and the dash-dot line for the satellite results.

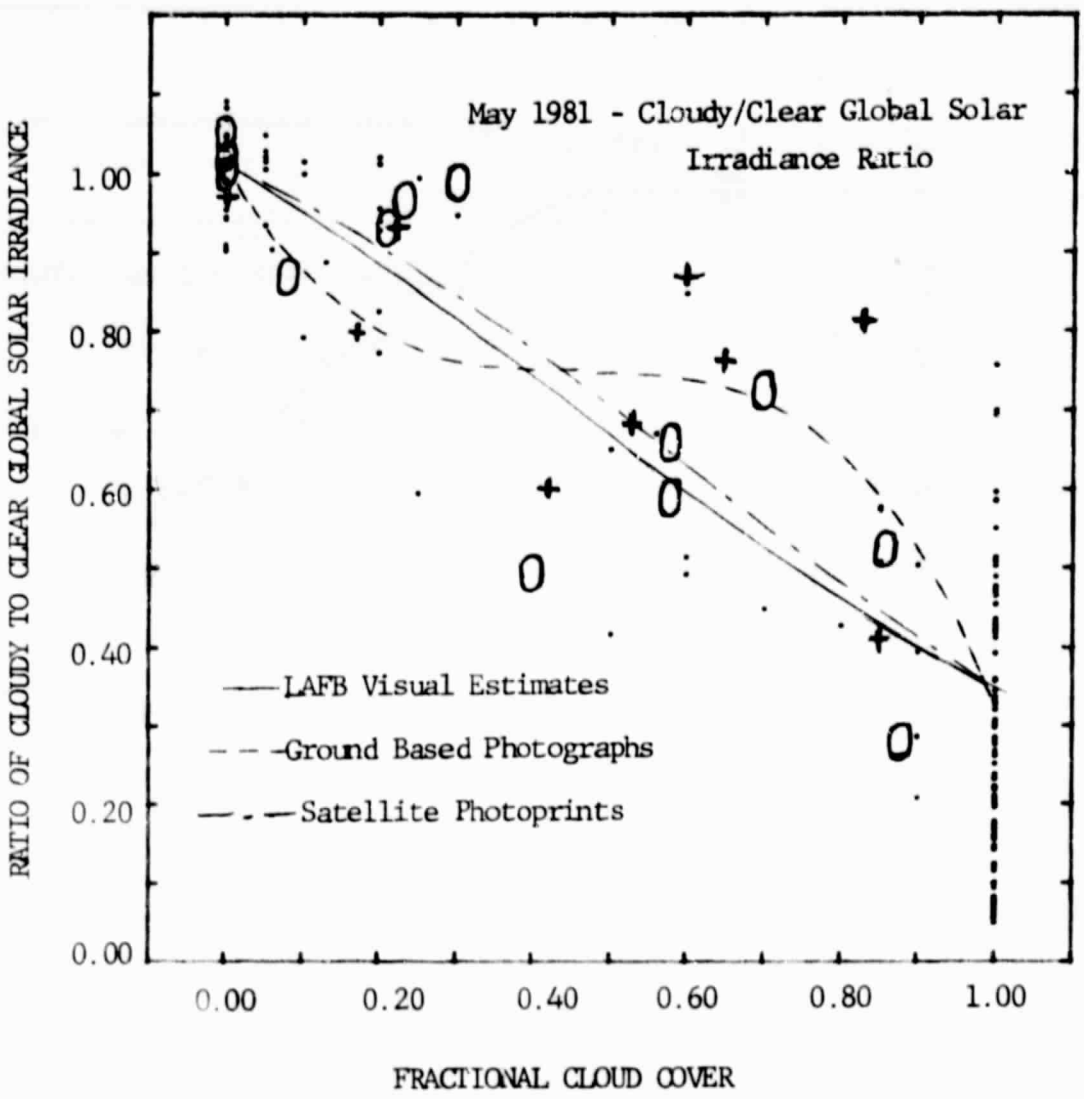

Figure 26. Cloudy to Clear Global Solar Irradiance Ratio versus Opaque Cloud Cover for the Month of May 1981. The dots represent the LAFB cloud fractions and each O represents satellite-derived fractions. Each + designates a ground-based photographic result. The solid line is the result of the least squares fit to the LAFB visual estimates using equation 2. The dashed line is for the ground based photograph results and the dash-dot line for the satellite results.

REFERENCES

Baker, D. G., 1979, "Solar Radiation Data Sources: Availability, Processing, and Quality Control," Solar Energy Measurements and Instrumentation, Engineering Summer Conference, July 9-10, The University of Michigan, College of Engineering.

Drummond, A. J., 1956, "On the Measurement of Sky Radiation," Arch. Meteor. Geophys. & Bioklim., 7, pp. 413-436.

Eppley Laboratory, Inc., Instructions for Installation and Operation of Diffuse Sky Radiation Instrumentation, Newport, RI, pp. 1-6.

Kuhn, W. R., 1979, "Modelling of Received Solar Radiation," Solar Energy Measurements and Instrumentation, Engineering Summer Conference, July 9-10, The University of Michigan, College of Engineering.

Lund, I. A., and Shanklin, M.D., 1972, "Photogrammetrically Determined Cloud-Free Lines-of-Sight Through the Atmosphere," J. Appl. Meteorol., 11, pp. 773-782.

Lund, I. A., Grantham, D. D., and Davis, R. E., 1980, "Estimating Probabilities of Cloud-Free Fields-of-View from the Earth Through the Atmosphere," J. Appl. Meteorol., 19, pp. 452-463.

Marquardt, D. W., 1963, "An Algorithm for Least-Squares Estimation of Nonlinear Parameters," J. Soc. Ind. Appl. Math., 11, pp. 431-441.

Ryzner, E., 1979, "Solar and Infrared Radiometers at Primary and Mobile Measurement Facilities," Solar Energy Measurements and Instrumentation, Engineering Summer Conference, July 9-10, The University of Michigan, College of Engineering.

Volz, F., 1974, "Economical Multispectral Sun Photometer for Measurements of Aerosol Extinction from 0.44 Microns to 1.6 Microns and Precipitable Water," Appl. Optics, 13 (8), pp. 1732-1733.